

Deep recurrent model for individualized prediction of Alzheimer's disease progression



Wonsik Jung^a, Eunji Jun^a, Heung-Il Suk^{a,b,*}, Alzheimer's Disease Neuroimaging Initiative^{a,b,1}

^a Department of Brain and Cognitive Engineering, Korea University, Seoul 02841, Republic of Korea

^b Department of Artificial Intelligence, Korea University, Seoul 02841, Republic of Korea

ARTICLE INFO

Keywords:

Disease Progression Modeling
 Alzheimer's Disease
 Deep Learning
 Recurrent Neural Networks
 Longitudinal Data
 Mild Cognitive Impairment
 Conversion-Time Prediction
 Cognitive tests
 Missing Value Imputation

ABSTRACT

Alzheimer's disease (AD) is known as one of the major causes of dementia and is characterized by slow progression over several years, with no treatments or available medicines. In this regard, there have been efforts to identify the risk of developing AD in its earliest time. While many of the previous works considered cross-sectional analysis, more recent studies have focused on the diagnosis and prognosis of AD with longitudinal or time series data in a way of disease progression modeling. Under the same problem settings, in this work, we propose a novel computational framework that can predict the phenotypic measurements of MRI biomarkers and trajectories of clinical status along with cognitive scores at multiple future time points. However, in handling time series data, it generally faces many unexpected missing observations. In regard to such an unfavorable situation, we define a secondary problem of estimating those missing values and tackle it in a systematic way by taking account of temporal and multivariate relations inherent in time series data. Concretely, we propose a deep recurrent network that jointly tackles the four problems of (i) missing value imputation, (ii) phenotypic measurements forecasting, (iii) trajectory estimation of a cognitive score, and (iv) clinical status prediction of a subject based on his/her longitudinal imaging biomarkers. Notably, the learnable parameters of all the modules in our predictive models are trained in an end-to-end manner by taking the morphological features and cognitive scores as input, with our circumspectly defined loss function. In our experiments over The Alzheimers Disease Prediction Of Longitudinal Evolution (TADPOLE) challenge cohort, we measured performance for various metrics and compared our method to competing methods in the literature. Exhaustive analyses and ablation studies were also conducted to better confirm the effectiveness of our method.

1. Introduction

Alzheimer's disease (AD) is a catastrophic and progressive neurodegenerative disease that is clinically characterized by the impairment of cognitive and functional abilities along with behavioral symptoms. It is known that AD is the most common cause of dementia, accounting for about 70% of age-related dementia (Alzheimer's Association, 2019). It is estimated that there are approximately 50 million AD patients around the world, and the figure will double by 2030 (Patterson, 2018), thus causing great social and economic burdens (Alzheimer's Association, 2019; Brookmeyer et al., 2007). Unfortunately, there is currently no pharmaceutical or clinical treatment available to reverse or cure the progression of AD (Gaugler et al., 2019; Marinescu et al., 2018). When considering the characteristics of patients with AD, the clinical symptoms that disturb the activities of daily living, such as memory loss,

language impediment, and other malfunctions, become apparent only after several years from the time that the brain is initially affected by the disease (Braak and Braak, 1996; Morris et al., 1996). For this reason, it is of great importance to identify the emergence of the disease at its earliest stage or predict the risk of emergence as early as possible.

In recent decades, leveraging the advances in machine learning, especially deep learning (Goodfellow et al., 2016; Suk, 2017), there have been efforts to formulate the task of neuroimaging-based early AD diagnosis or prognosis as regression and classification problems (Liu et al., 2018b; Suk et al., 2014; 2016; Zhang et al., 2011). On the one hand, many of the existing studies focused on cross-sectional data analysis for AD diagnosis (Cheng et al., 2017; Liu et al., 2018a; Suk and Shen, 2013; Suk et al., 2015). These studies showed reasonable performance in the clinical status prediction task, even though only baseline features were

* Corresponding author.

E-mail address: hisuk@korea.ac.kr (H.-I. Suk).

¹ Data used in preparation of this article were obtained from the Alzheimer's Disease Neuroimaging Initiative (ADNI) database (<http://www.loni.ucla.edu/ADNI>). As such, the investigators within the ADNI contributed to the design and implementation of ADNI and/or provided data but did not participate in analysis or writing of this report. A complete listing of ADNI investigators can be found at http://adni.loni.ucla.edu/wpcontent/uploads/how_to_apply/ADNI_Authorship_List.pdf.

<https://doi.org/10.1016/j.neuroimage.2021.118143>.

Received 7 August 2020; Received in revised form 15 March 2021; Accepted 13 April 2021

Available online 13 May 2021.

1053-8119/© 2021 The Author(s). Published by Elsevier Inc. This is an open access article under the CC BY-NC-ND license (<http://creativecommons.org/licenses/by-nc-nd/4.0/>)

used. However, they have limitations that did not properly model the progressive deterioration of the disease and different occurrence times for each individual, which are characteristics of AD.

On the other hand, in order to better utilize the available historical data, *i.e.*, longitudinal data, disease progression modeling (DPM) has drawn researchers' attention (Ghazi et al., 2019; Lee et al., 2019; Lorenzi et al., 2019; Nguyen et al., 2020; Peterson et al., 2017; Sukkar et al., 2012), especially for prediction of the time-to-conversion to the next clinical status in the AD spectrum. The AD progression generally involves not only the acceleration of regional volume atrophy (*e.g.*, the hippocampus, which is presumed to show the earliest morphological changes due to AD) but also increased enlargement of the ventricle over time (Nestor et al., 2008). These types of changes can be better captured from longitudinal data, which allows for learning the underlying temporal characteristics in the disease. By discovering such characteristics, a DPM may be possible to forecast the future changes in phenotypic measurements and predict the time of conversion in clinical statuses that are symptomatically categorized as cognitively normal (CN), mild cognitive impairment (MCI), and dementia (Mills and Tammes, 2014). In particular, a better understanding of the individual disease progression contributes to more accurate diagnosis, monitoring, and prognosis, which are respectively beneficial for early diagnosis, intervention, and personalized care (Oxtoby and Alexander, 2017). In this work, we focus on neuroimaging-based DPM for AD prognosis and time-to-conversion prediction in the AD spectrum.

For the DPM, conversion time prediction is critical, as it gives us meaningful information about the disease progression and the severity of the disease. It is much more challenging than just predicting whether the patient will progress to AD. Conversion time prediction in this study is analogous to survival analysis (Miller Jr, 2011; Oulhaj et al., 2009; Thung et al., 2018). Survival analysis is the study of time-to-event data, modeling the expected period until event occurrence (*e.g.*, disease status conversion) at a future time. Although conversion time prediction resembles survival analysis, they actually tackle the problems with different approaches. First, survival analysis focuses on predicting the probability of AD conversion at different future time points. However, conversion time prediction forecasts when the conversion of the disease will occur. For example, in general, probability methods (*e.g.*, Cox regression model) are used to access the survival problems, while conversion time prediction is based on typical regression methods (*e.g.*, least-squares regression model) (Thung et al., 2018). In this work, we investigate both approaches in devising the DPM for AD progression.

In the literature on survival analysis and related fields, DPM has been widely applied when the causes of diseases were not well-known, or various factors were involved. Although working with longitudinal data is useful for improving our knowledge of the disease, adding a temporal dimension entails different forms of difficulties in data analysis, such as increasing dimensionality, missing values, and time alignment problems (Ibrahim and Molenberghs, 2009). In a longitudinal dataset, there could be samples of subjects with one or two follow-ups ('short-term') and those of subjects with more frequent follow-ups ('long-term') after the first visit. Both scenarios have their own issues to be tackled. With short-term data, we might not suffer from missing measurements and data imbalance problems, but we are restricted from learning patterns of long-range dependence by nature, thus limited in building a reliable model for DPM (Ardekani et al., 2017; Fiot et al., 2014; Gray et al., 2012; Shi et al., 2017). Meanwhile, long-term longitudinal data are potentially better suited for DPM by allowing us to get better insights into the global patterns in disease progression (Aghili et al., 2018; Bilgel et al., 2015; 2016; Guerrero et al., 2016), but generally have issues of many missing measurements and time alignment, due to research or patients drop out or unexpected accidents, etc. (Petersen et al., 2010).

Some previous studies (Misra et al., 2009; Wei et al., 2016; Zhang et al., 2012) have been developed for MCI-to-AD conversion, which identified patients who will progress to AD. (Wei et al., 2016) used MRI thickness measures as features to predict MCI-to-AD conversion.

They used data at the baseline and up to 18 months (short-term samples). Meanwhile, (Misra et al., 2009) used longitudinal MRI data to extract the changes of brain atrophy for detecting MCI-to-AD conversion. However, this study employed short period follow-up data (up to 15 months). In addition, Zhang et al. also utilized a longer period of longitudinal MRI data up to 24 months to predict cognitive scores as well as the conversion of MCI patients by longitudinal feature selection method that extracts the brain regions across multiple time points (Zhang et al., 2012).

More recently, we have witnessed the potential of deep learning methods (Ghazi et al., 2019; Jung et al., 2019; Lee et al., 2019; Nguyen et al., 2020; Wang et al., 2018) for DPM thanks to their favorable characteristics of learning feature representations from data, rather than engineering feature manually. Especially, recurrent neural networks (RNNs) and their variants have been widely used because of their methodological ability to handle the time alignment issue among intra- and inter-subject trajectories. In particular, long short-term memory (LSTM) (Hochreiter and Schmidhuber, 1997) is one of the successful techniques to encode temporal patterns (Ghazi et al., 2019; Jung et al., 2019; Wang et al., 2018; Yoon et al., 2018) by capturing long-term dependencies among multivariate measurements over time with efficient gating-based operations (Gers and Schmidhuber, 2001; Gers et al., 1999). However, its use in DPM remains challenging due to the incomplete samples, *i.e.*, missing measurements in the data. For that reason, the previous works (Ghazi et al., 2019; Lipton et al., 2016; Nguyen et al., 2020; Wang et al., 2018; Yoon et al., 2018) have mostly involved the step of missing value imputation either as a means of preprocessing prior to training RNNs (Lipton et al., 2016; Wang et al., 2018) or by regarding it as a sub-task of the target model training for prediction (Yoon et al., 2018).

More insight for these approaches, Lipton et al. exploited RNNs with LSTM cells to diagnose the pediatric intensive care unit (PICU) from clinical time series data (Lipton et al., 2016). Wang et al. also used similar RNNs variants to predict future cognitive scores given 11 yearly observations (Wang et al., 2018). When training their method, all missing values of the patients' historical observations due to varying number of visits and uneven time intervals, were first imputed by simple mean or forward imputation methods (Lipton et al., 2016; Wang et al., 2018), disregarding both the temporal relations and multivariate relations of observations. Meanwhile, Ghazi et al. formulated the task of AD progression modeling by means of predicting changes in volumetric MRI biomarkers in a vanilla LSTM with peephole connections (Gers and Schmidhuber, 2000) added to all the gates (Ghazi et al., 2019). In contrast, all the missing values of longitudinal samples were initialized with zeros, and no further imputation update was conducted. Here, we named this model as PLSTM-Z. It is also noteworthy that for the clinical status prognosis, they built a separate classifier with linear discriminant analysis (LDA) by taking the predicted biomarker values from the trained PLSTM-Z as input features.

Since the performance of predictive models with preprocessing-based missing value imputation is highly dependent on the static values, *e.g.*, zeros and means, determined manually or statistically, some researchers have devoted their efforts to constructing adaptive and dynamic imputation models. For example, Yoon et al. focused on the task of missing value imputation and utilized a bi-directional RNN to better take into account temporal relations, but no relations among multivariate features, for mortality prediction with electronic health records (Yoon et al., 2018). Furthermore, Nguyen et al. employed a mean value across all time points for the missing value at the first time (*i.e.*, forward filling (Lipton et al., 2016)) and predicted the next missing values by means of MinimalRNN. However, there exists still a limitation to consider no feature-based relations (Nguyen et al., 2020). More recently, Cao et al. gave special attention to the task of missing values imputation in time series data (Cao et al., 2018). In particular, given a sequence of observations in a fixed time interval, they designed the LSTM model, the one in the original time order and the other in the

reversed time order, to maximally utilize the inherent temporal relations along with multivariate relations. However, due to the use of a time-reversed sequence, their imputation method is not applicable for disease progression modeling, *i.e.*, long-term prognosis utilizes current and more recently available data, but not future data.

Inspired by the recent work of dynamic imputation methods described above, in this work, we hypothesize that both multivariate and temporal relations inherent in longitudinal data could be informative to estimate missing values in devising DPM for AD. It is also believed that the appropriately imputed values help enhance the predictive power of a model for downstream tasks, *i.e.*, in our work, volumetric changes of MRI biomarkers, trajectories of a cognitive score, and clinical status prognosis over multiple time points ahead, thus making it possible to infer time-to-conversion in the AD spectrum. In these regards, we propose a unified framework that can (i) adaptively impute missing values ('*imputation module*'), (ii) encode imputed observations into latent representations via LSTM ('*encoding module*'), and (iii) predict future MRI volumetric measurements, trajectories of a cognitive score, and clinical statuses ('*prediction module*') over time in terms of the AD progression from a subject's historical measurements. Methodologically, we devise an imputation architecture that takes advantage of the encoded latent representations from an LSTM cell, *i.e.*, temporal relations, and utilizes multivariate relations among variables to infer missing values. For the temporal encoding in LSTM-Z (LSTM with zero imputation), we feed the *complete* observation, *i.e.*, replace the missing values with imputed ones, a mask vector that indicates which values are imputed, and the information of time-delay from the last observed times. All of these greatly help to better encode and capture temporal characteristics in a longitudinal sample for modeling disease progression. Further, we also design an objective function such that the network parameters of all the three modules can be trained jointly in an end-to-end manner.

We evaluated the performance of our proposed method using the longitudinal cohorts from 'The Alzheimers Disease Prediction Of Longitudinal Evolution (TADPOLE) Challenge'² in terms of (i) future volumetric biomarker regression, (ii) cognitive score regression, and (iii) clinical status classification, respectively. Furthermore, we conducted exhaustive analyses to verify the effectiveness of the proposed framework for AD progression in three aspects, namely, model perspective analysis, longitudinal stability analysis, and personalized analysis.

The main contributions of our work can be summarized as follows:

- We devise a novel deep recurrent network that jointly performs missing value imputation, forecasting of future MRI biomarker and cognitive score, and clinical status prognosis over multiple time points in a unified framework.
- A multi-objective function for the proposed imputation-encoding-prediction network is devised and optimized in an end-to-end manner.
- Compared to the competing methods considered in our experiments, our proposed method outperformed them in all metrics for imputation, regression, and classification.

This work extends the preliminary version published by (Jung et al., 2019) by revising the network architecture and performing further extensive experiments and analyses. Specifically, compared to the earlier work, the following extension and improvements have been made: first, we utilized the cognitive scores of Mini-Mental State Examination (MMSE) and Alzheimer's Disease Assessment Scale-Cognitive Subscale (ADAS-cog11 and ADAS-cog13) as input to the model along with the volumetric MRI features, and predicted the cognitive scores and the clinical labels over time. Moreover, we performed rigorous analyses for the experimental results with respect to the effect of multi-task learning,

conducted ablation studies concerning the composite objective function and justification for the proposed method, and compared multiple time points prediction results between our proposed method and competing methods. Lastly, we also conducted model analyses by interpreting the cell states of our encoding module.

2. Materials and preprocessing

In this work, we used the TADPOLE longitudinal cohort³ from the ADNI database, including ADNI-1, ADNI-2, and ADNI-GO. The main objective of the challenge was to track the progression of subjects with AD using MRI biomarkers, cognitive test scores, and clinical measurements. The dataset includes 1,500 kinds of longitudinal MRI biomarkers, *e.g.*, cortical thickness and cortical volume, from 1,737 patients (aged from 54.40 up to 91.40) with 12,741 visits at 22 different time points between 2003 and 2017 (Marinescu et al., 2018). The summary of the TADPOLE dataset is presented in Table A1 in Appendix A1.

As our main objective in this work is to predict the yearly progression, we considered 11 regular visits out of 22 total visits. In the TADPOLE dataset, the clinical groups were labeled as 342 AD, 417 CN, 310 EMCI (early MCI), 562 LMCI (late MCI), and 106 SMC (significant memory concern). Like the previous work (Ghazi et al., 2019; Jung et al., 2019), we merged the groups of CN and SMC into CN, and EMCI and LMCI into MCI, thus resulting in three categories: CN, MCI, and AD. Moreover, from the original TADPOLE dataset, we excluded subjects with no visit on the baseline or having less than 3 visits, resulting in a total of 691 subjects in the end. The number of longitudinal measurements ranges from 4 to 11 with 5.37 ± 2.46 (mean \pm std). The duration of sequences ranges from 36 to 120 with 64.40 ± 29.48 (mean \pm std). The detailed information of demographic and cognitive scores for samples used in our work is summarized in Table C1 over 11 yearly time points (see appendix C). Note that there are many missing observations in the MRI biomarkers and clinical labels over the selected dataset.

Although the TADPOLE dataset offers numerous kinds of biomarkers to forecast the AD status (Marinescu et al., 2018), by following previous studies (Albright and Alzheimer's Disease Neuroimaging Initiative and others, 2019; Ghazi et al., 2019; Iddi et al., 2019; Lu, 2019; Marinescu et al., 2019b; Oxtoby et al., 2018) in this paper, we considered the six volumetric features of ventricles, hippocampus, fusiform gyrus, middle temporal gyrus, entorhinal cortex, and whole-brain, extracted from the T1-weighted MRI that are shown in Fig. B1 and cognitive tests such as MMSE, ADAS-cog11, and ADAS-cog13. In the case of volumetric MRI features, we normalized the original values of the biomarkers with each subject's intracranial volume (ICV) to compensate for the inter-subject variability in brain size (Davis and Wright, 1977; Ghazi et al., 2019) and further conducted feature-wise linear normalization based on the min/max values to be in the range of $[-1, 1]$. Specifically, all features were min/max normalized on the training set. The validation and test values were normalized the same way to the training samples, thus for those values beyond the range of [min, max], the normalized values were also beyond the range of $[-1, 1]$ accordingly. To be more specific, we calculated the six min and max values for one-pair each MRI feature. We then normalized each training, validation, and test input features with their respective min-max values. For reference, we illustrated an example of morphological changes of six regions in a subject's brain, who experienced three clinical statuses during the 11-year period, in Fig. 1. In the case of cognitive scores, we normalized their values to be in the range of $[0, 1]$.

3. Proposed method

In this work, we propose a novel framework for AD progression modeling with incomplete longitudinal data. Specifically, our proposed

² <https://tadpole.grand-challenge.org/>

³ Available at <https://tadpole.grand-challenge.org/Data/>

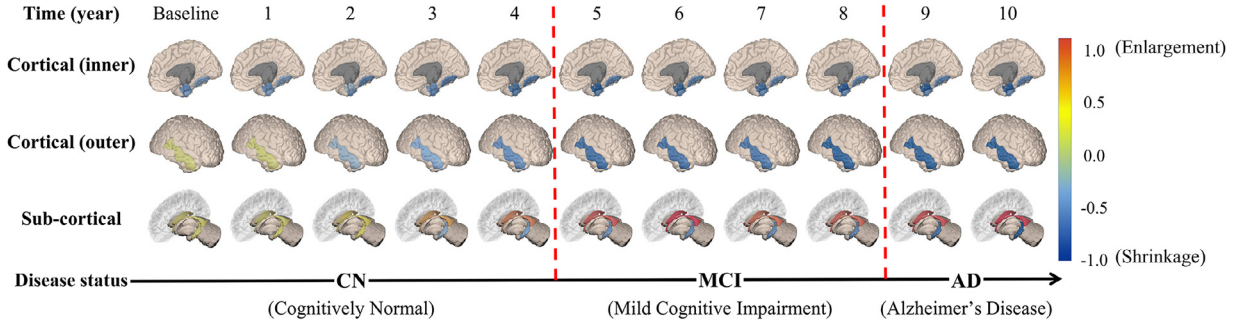


Fig. 1. An example of morphological changes of pre-selected regions in a subject's brain. The color-coded values indicate the amount of volume changes from a baseline time point. The darker color of either blue or red, the more shrunk or enlarged volume from a baseline time point.

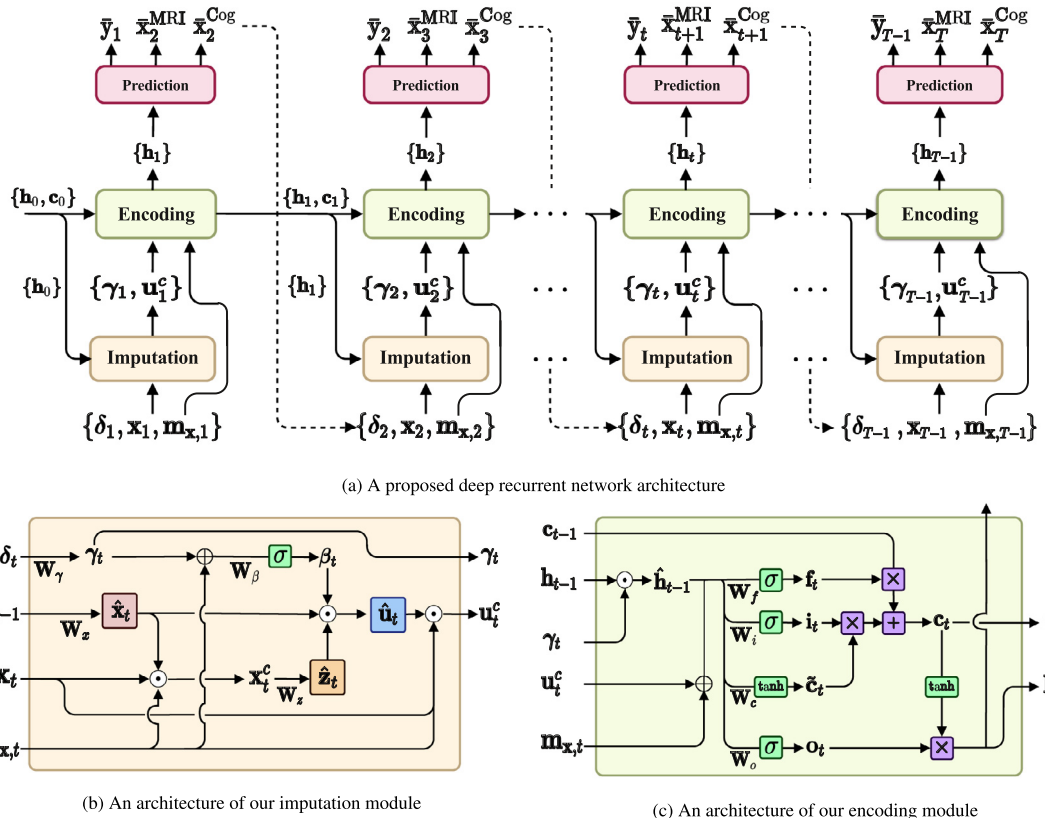


Fig. 2. (a) The architecture of the proposed method combines three modules, i.e., imputation, encoding, and prediction. The modules impute the missing values of the current input, forecast both the biomarker values and cognitive scores of the next time point and predict the clinical status of the current time point. (b) Operations to consider the feature-based relations and temporal relations in estimating missing values. (c) A variant of a vanilla LSTM unit with γ and $m_{x,t}$. For simplicity, the biases are excluded. If unobserved, the predicted values are used as the input of the next time step, which is denoted as dotted arrows. Solid arrows indicate the process of architecture.

method is composed of three modules, namely, an imputation module, encoding module, and prediction module, as illustrated in Fig. 2a. At a certain time point, the imputation module first estimates missing values using the encoded latent representations from the previous time point in a deep recurrent network, as well as the multivariate relations among the observed values of the current time point. Second, the encoding module receives the *complete* observation with the missing values replaced by imputed ones, a mask vector that indicates which values are imputed, and the time-delay information from the time interval, representing a duration from the last observed time points. Through this process, the proposed network encodes and captures underlying temporal characteristics in the given longitudinal data. Lastly, the encoded representations are further transformed to forecast both the volumetric measurements and cognitive scores of the

next time point and predict the clinical status of the current time point.

3.1. Notations

Throughout the paper, we denote matrices as boldface uppercase letters, vectors as boldface lowercase letters, and scalars as normal italic letters. For a matrix A , its (i, j) -th element and the i -th column are denoted as $A(i, j)$ and \mathbf{a}_i , respectively. For a vector \mathbf{a} , its i -th element is denoted as $a(i)$. For a better understanding of all notations, we summarize the mathematical notations including their intuitive descriptions, dimensionality, and mapping functions in Table 1.

Assume that a set of multivariate time series of D variables over T times from N number of subjects are given $\{\mathbf{X}^{(n)}, \mathbf{Y}^{(n)}\}_{n=1}^N$, where $\mathbf{X}^{(n)} =$

Table 1

A summary of mathematical notations in our proposed method.

Symbols	Description	Dimensionality (\mathbb{R})	Mapping function	Equations
N, T	the number of samples (batch size), time points	$64, 10$		
H, D, K	the number of hidden units, variables, classes	$64, 9, 3$		
\oplus	concatenation operator			
\odot	element-wise multiplication operator			
$\sigma(\cdot)$	logistic sigmoid function			
$\mathbf{m}_{y,t}$	label mask vector	$N \times K$		
s_t	an indicator when the observations were acquired	T		
<i>Longitudinal subset</i>				
\mathbf{X}, \mathbf{Y}	input features, clinical status of total patients	$N \times D \times T, N \times K \times T$		
$\mathbf{x}_t = \{\mathbf{x}_t^{\text{MRI}}, \mathbf{x}_t^{\text{Cog}}\}, \mathbf{y}_t$	MR volumetric and cognitive test features, label at time t	$N \times D, N \times K$		
<i>The variables of missing value imputation</i>				
$\hat{\mathbf{x}}_t$	temporal relations variable	$N \times D \times 1$	$f_x : \mathbb{R}^{H \times 1} \rightarrow \mathbb{R}^{D \times 1}$	$\hat{\mathbf{x}}_t = f_x(\mathbf{h}_{t-1}) = \mathbf{W}_x \mathbf{h}_{t-1} + \mathbf{b}_x$
\mathbf{x}_t^c	temporary vector, estimated from the temporal relations	$N \times D \times 1$		$\mathbf{x}_t^c = \mathbf{m}_{x,t} \odot \mathbf{x}_t + (\mathbf{1} - \mathbf{m}_{x,t}) \odot \hat{\mathbf{x}}_t$
$\hat{\mathbf{z}}_t$	multivariate relations variable	$N \times D \times 1$	$f_z : \mathbb{R}^{D \times 1} \rightarrow \mathbb{R}^{D \times 1}$	$\hat{\mathbf{z}}_t = f_z(\mathbf{x}_t^c) = \mathbf{W}_z \mathbf{x}_t^c + \mathbf{b}_z$
$\hat{\mathbf{u}}_t$	estimates using an interpolation between $\hat{\mathbf{x}}_t$ and $\hat{\mathbf{z}}_t$	$N \times D \times 1$		$\hat{\mathbf{u}}_t = \beta_t \odot \hat{\mathbf{z}}_t + (1 - \beta_t) \odot \hat{\mathbf{x}}_t$
\mathbf{u}_t^c	complete observation vector	$N \times D \times 1$		$\mathbf{u}_t^c = \mathbf{m}_{x,t} \odot \mathbf{x}_t + (\mathbf{1} - \mathbf{m}_{x,t}) \odot \hat{\mathbf{u}}_t$
<i>The variables related to missing patterns</i>				
$\mathbf{M}_x = \mathbf{m}_{x,t}$	input masking vector	$N \times D \times 1$		
δ_t	time delay vector	$N \times D \times 1$		
\mathbf{h}_{t-1}	initial hidden state	$N \times H \times 1$		
$\gamma_t \in (0, 1]^D$	temporal decay factor for temporal relations	$N \times H \times 1$	$f_{\gamma_t} : \mathbb{R}^{D \times 1} \rightarrow \mathbb{R}^{H \times 1}$	$\gamma_t = f_{\gamma_t}(\delta_t) = \exp\{-\max(0, \mathbf{W}_{\gamma_t}^\top \delta_t + \mathbf{b}_{\gamma_t})\}$
$\gamma_z \in (0, 1]^D$	temporal decay factor for multivariate relations	$N \times D \times 1$	$f_{\gamma_z} : \mathbb{R}^{D \times 1} \rightarrow \mathbb{R}^{D \times 1}$	$\gamma_z = f_{\gamma_z}(\delta_t) = \exp\{-\max(0, \mathbf{W}_{\gamma_z}^\top \delta_t + \mathbf{b}_{\gamma_z})\}$
$\beta_t \in (0, 1)^D$	weighting coefficient vector	$N \times D \times 1$	$f_\beta : \mathbb{R}^{2D \times 1} \rightarrow \mathbb{R}^{D \times 1}$	$\beta_t = f_\beta([\gamma_z \oplus \mathbf{m}_{x,t}]) = \sigma(\mathbf{W}_\beta \odot [\gamma_z \oplus \mathbf{m}_{x,t}] + \mathbf{b}_\beta)$
<i>The variables of Recurrent Temporal Encoding</i>				
$\hat{\mathbf{h}}_{t-1}$	previous hidden state considered by temporal decay factor γ_t	$N \times H \times 1$		$\hat{\mathbf{h}}_{t-1} = \mathbf{h}_{t-1} \odot \gamma_t$
\mathbf{f}_t	forget gate	$N \times H \times 1$	$f_{fo} : \mathbb{R}^{H \times 1} \rightarrow \mathbb{R}^{H \times 1}$	$\mathbf{f}_t = f_{fo}([\mathbf{u}_t^c \oplus \mathbf{m}_{x,t}]) = \sigma(\mathbf{W}_{fo} \odot [\hat{\mathbf{h}}_{t-1}, \mathbf{u}_t^c \oplus \mathbf{m}_{x,t}] + \mathbf{b}_{fo})$
\mathbf{i}_t	input gate	$N \times H \times 1$	$f_i : \mathbb{R}^{H \times 1} \rightarrow \mathbb{R}^{H \times 1}$	$\mathbf{i}_t = f_i([\mathbf{u}_t^c \oplus \mathbf{m}_{x,t}]) = \sigma(\mathbf{W}_i \odot [\hat{\mathbf{h}}_{t-1}, \mathbf{u}_t^c \oplus \mathbf{m}_{x,t}] + \mathbf{b}_i)$
\mathbf{o}_t	output gate	$N \times H \times 1$	$f_o : \mathbb{R}^{H \times 1} \rightarrow \mathbb{R}^{H \times 1}$	$\mathbf{o}_t = f_o([\mathbf{u}_t^c \oplus \mathbf{m}_{x,t}]) = \sigma(\mathbf{W}_o \odot [\hat{\mathbf{h}}_{t-1}, \mathbf{u}_t^c \oplus \mathbf{m}_{x,t}] + \mathbf{b}_o)$
$\tilde{\mathbf{c}}_t$	update gate	$N \times H \times 1$	$f_c : \mathbb{R}^{H \times 1} \rightarrow \mathbb{R}^{H \times 1}$	$\tilde{\mathbf{c}}_t = f_c([\mathbf{u}_t^c \oplus \mathbf{m}_{x,t}]) = \tanh(\mathbf{W}_c \odot [\hat{\mathbf{h}}_{t-1}, \mathbf{u}_t^c \oplus \mathbf{m}_{x,t}] + \mathbf{b}_c)$
\mathbf{c}_t	cell state	$N \times H \times 1$		$\mathbf{c}_t = \mathbf{f}_t \odot \mathbf{c}_{t-1} + \mathbf{i}_t \odot \tilde{\mathbf{c}}_t$
\mathbf{h}_t	hidden state at time t	$N \times H \times 1$		$\mathbf{h}_t = \mathbf{o}_t \odot \tanh(\mathbf{c}_t)$
<i>Learnable parameters</i>				
$\mathbf{W}_x, \mathbf{W}_{\gamma_t} / \mathbf{W}_z, \mathbf{W}_{\gamma_z}, \mathbf{W}_\beta$	Weight in imputation module	$D \times H / D \times D / D \times 2D$		
$\mathbf{b}_x, \mathbf{b}_z, \mathbf{b}_{\gamma_t}, \mathbf{b}_\beta / \mathbf{b}_{\gamma_z}$	Bias in imputation module	$D \times 1 / H \times 1$		
$\mathbf{W}_{fo,i}, \mathbf{W}_{ii}, \mathbf{W}_{ci}, \mathbf{W}_{oi}$	Weight of input in encoding module	$H \times 2D$		
$\mathbf{W}_{fob}, \mathbf{W}_{ih}, \mathbf{W}_{ch}, \mathbf{W}_{oh}$	Weight of hidden in encoding module	$H \times H$		
$\mathbf{b}_{fo,i}, \mathbf{b}_{ii}, \mathbf{b}_{ci}, \mathbf{b}_{oi}$	Bias of input in encoding module	$H \times 1$		
$\mathbf{b}_{fob}, \mathbf{b}_{ih}, \mathbf{b}_{ch}, \mathbf{b}_{oh}$	Bias of hidden in encoding module	$H \times 1$		

\mathbf{W}_z initialized the diagonal elements to take into account multivariate relations; Each of the weight vectors i.e., $\mathbf{W}_{fo,o}, \mathbf{W}_i, \mathbf{W}_c$ and \mathbf{W}_o consists of 2 kinds of internal vectors, $\mathbf{W}_{(gate)i}$ and $\mathbf{W}_{(gate)h}$ ($\{fo, i, c, o\} \in \text{gate}$).

$[\mathbf{x}_1^{(n)}, \dots, \mathbf{x}_t^{(n)}, \dots, \mathbf{x}_T^{(n)}] \in \mathbb{R}^{D \times T}$, $\mathbf{Y}^{(n)} = [\mathbf{y}_1^{(n)}, \dots, \mathbf{y}_t^{(n)}, \dots, \mathbf{y}_T^{(n)}] \in \{0, 1\}^{K \times T}$, and K denotes the number of classes considered in a target task. In our case, it corresponds to the clinical state of a patient, i.e., CN, MCI, and AD. To limit clutter, hereafter we omit the superscript (n) unless it is unclear in the context. Additionally, to clearly define two types of features, we employ input features $\mathbf{x}_t = \{\mathbf{x}_t^{\text{MRI}}, \mathbf{x}_t^{\text{Cog}}\}$, where $\mathbf{x}_t^{\text{MRI}}$ is MR volumetric features and $\mathbf{x}_t^{\text{Cog}}$ is cognitive tests features⁴.

⁴ There could be a concern of exploiting the cognitive scores to make a clinical status prediction because it carries a certain amount of information related to the clinician's decision, i.e., ground truth. Surely, when it is possible, the cognitive scores are an important source to better estimate the clinical status of a patient, similar to the previous work in (Ghazi et al., 2019; Iddi et al., 2019; Marinescu et al., 2019b; Nguyen et al., 2020; Oxtoby et al., 2018; Venkatraghavan et al., 2019). However, in regard to the progression modeling, especially in

As both \mathbf{X} and \mathbf{Y} are characterized with sparsity properties, we tackle the missing values by utilizing a mask vector, indicating whether a value is observed or not. Specifically, to inform the model which input features or labels are observed (or missing), we utilized mask vector as two auxiliary variables, i.e., input mask vector and label mask vector denoted as $\mathbf{M}_x \in \mathbb{R}^{D \times T}$ and $\mathbf{m}_y \in \mathbb{R}^{K \times T}$. Another consideration in addressing the missing data is to exploit a time interval between two observed data. In fact, such information delivers a piece of useful information for missing value imputation and latent feature representation. Thus, we accommodate this information by further devising a time delay matrix $\Delta \in \mathbb{R}^{D \times T}$ derived from $\mathbf{s} \in \mathbb{R}^T$, indicating the time interval of the observation. Here, we represent the elements of Δ as $\Delta(d, t)$ and $\delta_t \in \mathbb{R}^{D \times 1}$, denoted

making predictions over a long period, the cognitive scores will not be available definitely for future time points.

as follows:

$$\Delta(d, t) = \begin{cases} s(t) - s(t-1) + \Delta(d, t-1) & \text{if } t > 1, M_x(d, t-1) = 0, \\ s(t) - s(t-1) & \text{if } t > 1, M_x(d, t-1) = 1, \\ 1 & \text{if } t = 1. \end{cases}$$

In summary, we define the representations of informative missing patterns (Che et al., 2018), i.e., mask vector and time delay matrix. By exploiting these representations, we assumed that our network capable of not only capturing the long-term temporal dependencies of time series observations but also employing the missing patterns to enhance the imputation results.

3.2. Missing values imputation

We design an architecture that jointly exploits temporal and multivariate relations for imputation. Our imputation module is based on a deep recurrent neural network, which becomes an encoding module as described in Section 3.3. Specifically, we take the hidden state values of a recurrent network for the context of temporal relations in a given sequence.

To satisfy the above our assumption, we initially obtain the estimates from temporal relations as follows. At time t , the previous temporal context information up to $(t-1)$ is encoded in the hidden state \mathbf{h}_{t-1} of an encoding module. From the hidden state $\mathbf{h}_{t-1} \in \mathbb{R}^{H \times 1}$, where H is the number of hidden units, we first use the temporal relations for the estimation of between the MRI measurements and cognitive scores of the current time t as follows:

$$\hat{\mathbf{x}}_t = f_x(\mathbf{h}_{t-1}) = \mathbf{W}_x \mathbf{h}_{t-1} + \mathbf{b}_x \quad (1)$$

where $f_x : \mathbb{R}^{H \times 1} \rightarrow \mathbb{R}^{D \times 1}$ is a feed forward network served as a mapping function, while $\mathbf{W}_x \in \mathbb{R}^{D \times H}$ and $\mathbf{b}_x \in \mathbb{R}^{D \times 1}$ are learnable parameters of such a function. For clarity, we omit the mapping function for the rest of the equations while defined the detail of those mapping functions in Table 1.

Then, by exploiting the masking vector $\mathbf{m}_{x,t} \in \mathbb{R}^{D \times 1}$, we obtain a temporary vector $\mathbf{x}_t^c \in \mathbb{R}^{D \times 1}$ by replacing the missing values with those estimated from the temporal relations, while maintaining the observed both MR features and cognitive scores as follows:

$$\mathbf{x}_t^c = \mathbf{m}_{x,t} \odot \mathbf{x}_t + (\mathbf{1} - \mathbf{m}_{x,t}) \odot \hat{\mathbf{x}}_t \quad (2)$$

where \odot denotes an element-wise multiplication operator.

Henceforth, in order to accommodate the multivariate relations, we consider the MRI features as well as cognitive scores of the imputed temporal vector \mathbf{x}_t^c in Eq. (2), by introducing learnable parameters $\mathbf{W}_z \in \mathbb{R}^{D \times D}$ and $\mathbf{b}_z \in \mathbb{R}^{D \times 1}$ as follows:

$$\hat{\mathbf{z}}_t = \mathbf{W}_z \mathbf{x}_t^c + \mathbf{b}_z. \quad (3)$$

Here, we initialized the diagonal elements of \mathbf{W}_z with zeros to take into account multivariate relations in the missing value imputation module. Consequently, we aim to model relations how much one variable relates to other variables in \mathbf{x}_t^c . After deriving two imputed vectors, \mathbf{x}_t^c and $\hat{\mathbf{z}}_t$, by considering temporal and multivariate relations, we further consider the missing value estimates based on the temporal relations by exploiting the time interval δ_t between consecutive observations (Che et al., 2018). This time interval is fed into the temporal decay factor for temporal relation $\gamma_t \in (0, 1]^{H \times 1}$ as follows:

$$\gamma_t = \exp\{-\max(\mathbf{0}, \mathbf{W}_{\gamma_t}^\top \delta_t + \mathbf{b}_{\gamma_t})\} \quad (4)$$

where $\mathbf{W}_{\gamma_t} \in \mathbb{R}^{D \times H}$ and $\mathbf{b}_{\gamma_t} \in \mathbb{R}^{H \times 1}$ are tunable parameters. As stated to the missing patterns in Section 3.1, there are two sources of information, the masking vector $\mathbf{m}_{x,t}$ and the temporal decay factor γ_t are derived from time delay matrix δ_t . In order to consider the robustness of the missing value estimates, we further consider combining these two vectors by introducing a weighting coefficient vector that is dynamically determined, based on the missing patterns. To do this, we newly define

the temporal decay factor $\gamma_x \in \mathbb{R}^{D \times 1}$ in terms of weight coefficient vector as follows

$$\gamma_x = \exp\{-\max(\mathbf{0}, \mathbf{W}_{\gamma_x}^\top \delta_t + \mathbf{b}_{\gamma_x})\} \quad (5)$$

where $\mathbf{W}_{\gamma_x} \in \mathbb{R}^{D \times D}$ and $\mathbf{b}_{\gamma_x} \in \mathbb{R}^{D \times 1}$ are learnable parameters. Subsequently, combining this time decay factor with a masking vector via concatenation, we compute the weighting coefficient vector $\beta_t \in \mathbb{R}^{D \times 1}$ as follows:

$$\beta_t = \sigma(\mathbf{W}_\beta \odot [\gamma_x \oplus \mathbf{m}_{x,t}] + \mathbf{b}_\beta) \quad (6)$$

where $\mathbf{W}_\beta \in \mathbb{R}^{D \times 2D}$ and $\mathbf{b}_\beta \in \mathbb{R}^{D \times 1}$ are learnable parameters, σ denotes a logistic sigmoid function to guarantee that the coefficients are in the range of (0,1) and \oplus denotes the concatenation operation. Thus, $\beta_t \in \mathbb{R}^{D \times 1}$ carries the integrated information about the time decay factor $\gamma_x \in \mathbb{R}^{D \times 1}$ and the missing patterns at the current time step. With this weighting coefficient vector β_t , we finally estimate the missing values using an interpolation between $\hat{\mathbf{x}}_t$ and $\hat{\mathbf{z}}_t$

$$\hat{\mathbf{u}}_t = \beta_t \odot \hat{\mathbf{z}}_t + (1 - \beta_t) \odot \hat{\mathbf{x}}_t. \quad (7)$$

Through Eq. (7), missing values are estimated using interpolation between temporal relations and multivariate relations. Consequently, we obtain the ‘complete’ observation vector \mathbf{u}_t^c by replacing the missing values with the estimates in Eq. (8)

$$\mathbf{u}_t^c = \mathbf{m}_{x,t} \odot \mathbf{x}_t + (1 - \mathbf{m}_{x,t}) \odot \hat{\mathbf{u}}_t. \quad (8)$$

3.3. Recurrent temporal encoding and multi-task prediction

After imputing the missing values, we exploit a deep recurrent network for temporal encoding. Here, to better reflect the existence of missing values in an observation, we devise a novel computational mechanism, i.e., a variant of a vanilla LSTM cell with temporal decay factor γ_t and mask vector $\mathbf{m}_{x,t}$. In other words, the complete value \mathbf{u}_t^c in Eq. (8) is fed into the recurrent model.

First, as in the imputation module, we use the time delay information in δ_t , which is one of the important sources for temporal patterns (Che et al., 2018). That is, although the temporal context information up to the previous time $(t-1)$ is represented in the hidden state \mathbf{h}_{t-1} of a recurrent network, their influence in encoding with the current observation \mathbf{u}_t^c should be treated in different ways depending on when the ‘real’ last observation was acquired. Therefore, we use this crucial information with a temporal decaying factor γ_t in Eq. (4) before embedding with the current observation \mathbf{u}_t^c as follows:

$$\hat{\mathbf{h}}_{t-1} = \mathbf{h}_{t-1} \odot \gamma_t. \quad (9)$$

Through Eq. (9), hidden representation \mathbf{h}_{t-1} reflects the temporal patterns for missing observation. Besides, we also feed the masking vector $\mathbf{m}_{x,t}$ to the encoding module to let the model know which values are the imputed ones estimated from our imputation module. By employing temporal patterns and masking vectors, we consider that our model can capture missing patterns and further enhance the representation ability regardless of the missing observation.

Before describing the modified gating operation of the LSTM, we introduce the role of the three gates in Vanilla LSTM, i.e., forget gate \mathbf{f}_t , input gate \mathbf{i}_t , and output gate \mathbf{o}_t , and a memory cell state \mathbf{c}_t . These three gates communicate with each other to manage the stream of information. Specifically, the forget gate \mathbf{f}_t decides what information should be erased or kept, the input gate receives the new information through the candidate cell state $\tilde{\mathbf{c}}_t$ to update the cell state, and the output gate protects other units from irrelevant memory information and filters the information so that the model considers information relevant to the downstream task.

Concretely, the internal operations in our encoding module are as follows:

$$\mathbf{f}_t = \sigma(\mathbf{W}_{f,o} \odot [\hat{\mathbf{h}}_{t-1}, \mathbf{u}_t^c \oplus \mathbf{m}_{x,t}] + \mathbf{b}_{f,o})$$

$$\begin{aligned}\mathbf{i}_t &= \sigma(\mathbf{W}_i \odot [\hat{\mathbf{h}}_{t-1}, \mathbf{u}_t^c \oplus \mathbf{m}_{x,t}] + \mathbf{b}_i) \\ \tilde{\mathbf{c}}_t &= \tanh(\mathbf{W}_c \odot [\hat{\mathbf{h}}_{t-1}, \mathbf{u}_t^c \oplus \mathbf{m}_{x,t}] + \mathbf{b}_c) \\ \mathbf{c}_t &= \mathbf{f}_t \odot \mathbf{c}_{t-1} + \mathbf{i}_t \odot \tilde{\mathbf{c}}_t \\ \mathbf{o}_t &= \sigma(\mathbf{W}_o \odot [\hat{\mathbf{h}}_{t-1}, \mathbf{u}_t^c \oplus \mathbf{m}_{x,t}] + \mathbf{b}_o) \\ \mathbf{h}_t &= \mathbf{o}_t \odot \tanh(\mathbf{c}_t)\end{aligned}$$

where $\{\mathbf{W}_{fo}, \mathbf{W}_i, \mathbf{W}_c, \mathbf{W}_o, \mathbf{b}_{fo}, \mathbf{b}_i, \mathbf{b}_c, \mathbf{b}_o\}$ are the learnable parameters of our modified LSTM cell. $\mathbf{f}_t, \mathbf{i}_t, \tilde{\mathbf{c}}_t$, and \mathbf{o}_t represent the outputs of the forget, input, update, output gates, respectively. Specifically, each of the weight vectors, i.e., $\mathbf{W}_f, \mathbf{W}_i, \mathbf{W}_c$, and \mathbf{W}_o , consists of two kinds of internal vectors, $\mathbf{W}_{(gate)i} \in \mathbb{R}^{H \times 2D}$ and $\mathbf{W}_{(gate)h} \in \mathbb{R}^{H \times H}$, where $gate \in \{f, i, c, o\}$. Besides, each of the bias vectors has the same conditions. Here, i and h denote the marker, where weight vector is connected with input $\mathbf{u}_t^c \oplus \mathbf{m}_{x,t}$ or temporal context information $\hat{\mathbf{h}}_{t-1}$, respectively. The computation process is as follows:

$$\begin{aligned}\mathbf{i}_t &= \sigma(\mathbf{W}_f \odot [\hat{\mathbf{h}}_{t-1}, \mathbf{u}_t^c \oplus \mathbf{m}_{x,t}] + \mathbf{b}_f) \\ &= \sigma(\mathbf{W}_{fh} \odot \hat{\mathbf{h}}_{t-1} + \mathbf{b}_{fh} + \mathbf{W}_{fi} \odot (\mathbf{u}_t^c \oplus \mathbf{m}_{x,t}) + \mathbf{b}_{fi})\end{aligned}$$

Based on the hidden state representation \mathbf{h}_t from the encoding module, our prediction module produces three outcomes, i.e., the MRI measurements $\bar{\mathbf{x}}_{t+1}^{\text{MRI}}$, the cognitive tests $\bar{\mathbf{x}}_{t+1}^{\text{Cog}}$ of the next time point, and the clinical state $\bar{\mathbf{y}}_t$ of the current time point. We use simple linear and logistic regression models for each of the outcomes as follows:

$$\bar{\mathbf{x}}_{t+1}^{\text{MRI}} = \mathbf{W}_{\text{MRI}} \mathbf{h}_t + \mathbf{b}_{\text{MRI}} \quad (10)$$

$$\bar{\mathbf{x}}_{t+1}^{\text{Cog}} = \mathbf{W}_{\text{Cog}} \mathbf{h}_t + \mathbf{b}_{\text{Cog}} \quad (11)$$

$$\bar{\mathbf{y}}_t = \text{softmax}(\mathbf{W}_y \mathbf{h}_t + \mathbf{b}_y) \quad (12)$$

where $\mathbf{W}_{\text{MRI}}, \mathbf{W}_{\text{Cog}}, \mathbf{W}_y, \mathbf{b}_{\text{MRI}}, \mathbf{b}_{\text{Cog}}$, and \mathbf{b}_y are parameters. Thus, our prediction module is connected with the encoding module, and the parameters can be tuned jointly with those of the encoding module. From a learning standpoint, this prediction module takes advantage of a multi-task learning strategy for more predictive representations, comparable to the work of (Ghazi et al., 2019), where they first conducted MRI measurements forecasting and then built an independent classifier for clinical status prediction. In contrast to (Ghazi et al., 2019) which utilized MRI measurements only, we employed both MRI measurements and cognitive scores. In Section 5.1, we present the validity of our multi-task learning by comparing it with the counterpart single-task learning.

3.4. Learning

We defined a composite loss function for the joint training of the three modules, i.e., missing value imputation, temporal encoding, and output prediction. Specifically, for the imputation loss $\mathcal{L}_{\text{imputation}}$, we measure the similarity between the observed data and the imputed data by the mean absolute error (MAE) from three different perspectives, i.e., temporal relations in Eq. (1), multivariate relations in Eq. (3), and composite relations in Eq. (7).

$$\mathcal{L}_{\text{imputation}} = \sum_{t=1}^T (|\tilde{\mathbf{x}}_t - \hat{\mathbf{x}}_t| + |\tilde{\mathbf{x}}_t - \hat{\mathbf{z}}_t| + |\tilde{\mathbf{x}}_t - \hat{\mathbf{u}}_t|) \odot (1 - \tilde{\mathbf{m}}_{x,t}) \quad (13)$$

where $\tilde{\mathbf{x}}_t = \mathbf{x}_t \odot \mathbf{m}_{x,t}$ and $\tilde{\mathbf{m}}_{x,t}$ is a masking matrix of random removal from observations for imputation module training only. Empirically, when compared with a loss defined only with the final imputed values \mathbf{u}_x^c in Eq. (8), i.e., $|\tilde{\mathbf{x}}_t - \mathbf{u}_x^c|$, the joint loss in Eq. (13) enhanced the stability and speed in training.

As for the MRI biomarker prediction loss \mathcal{L}_{MRI} , we assessed the correspondence between the model prediction $\bar{\mathbf{x}}_{t+1}^{\text{MRI}}$ and the future real MRI measurements $\mathbf{x}_{t+1}^{\text{MRI}}$ by using the mean square error (MSE) as follows:

$$\mathcal{L}_{\text{MRI}} = \sum_{t=1}^{T-1} (\mathbf{x}_{t+1}^{\text{MRI}} \odot \mathbf{m}_{x,t+1} - \bar{\mathbf{x}}_{t+1}^{\text{MRI}} \odot \mathbf{m}_{x,t+1})^2. \quad (14)$$

Likewise, as for the cognitive scores prediction loss \mathcal{L}_{Cog} , we evaluated the correspondence between the model prediction $\bar{\mathbf{x}}_{t+1}^{\text{Cog}}$ and the real cognitive test measurements $\mathbf{x}_{t+1}^{\text{Cog}}$ as follows:

$$\mathcal{L}_{\text{Cog}} = \sum_{t=1}^{T-1} (\mathbf{x}_{t+1}^{\text{Cog}} \odot \mathbf{m}_{x,t+1} - \bar{\mathbf{x}}_{t+1}^{\text{Cog}} \odot \mathbf{m}_{x,t+1})^2. \quad (15)$$

Lastly, for the clinical prediction, we exploited the focal cross-entropy loss \mathcal{L}_y (Lin et al., 2017) due to the imbalance in samples among the class labels:

$$\mathcal{L}_y = - \sum_{t=1}^{T-1} \mathbf{m}_{y,t} \left[\sum_{k=1}^K y_t(k) (1 - \bar{y}_t(k))^\epsilon \log(\bar{y}_t(k)) \right] \quad (16)$$

where ϵ is a hyperparameter ($\epsilon \geq 0$). Therefore, we define the overall loss function $\mathcal{L}_{\text{total}}$ as follows:

$$\mathcal{L}_{\text{total}} = \alpha \mathcal{L}_{\text{imputation}} + \zeta (\mathcal{L}_{\text{MRI}} + \mathcal{L}_{\text{Cog}}) + \xi \mathcal{L}_y \quad (17)$$

where α , ζ , and ξ are the hyperparameters to weight the corresponding losses. The optimization of this loss function allows us to train all the parameters of the three modules, i.e., imputation, encoding, and prediction, via stochastic gradient descent in an end-to-end manner. Note that the objective functions are chosen differently depending on tasks from the experimental results, i.e., MAE for imputation and MSE for regression.

4. Experimental results and analysis

4.1. Experimental settings

We validated the effectiveness of the proposed framework that systematically unifies data-driven missing value imputation and multi-task learning for AD progression modeling in tasks of missing value imputation at the current time and both MRI biomarker and clinical test scores forecasting, as well as the clinical status prediction, we made predictions for every time point (with a one-year interval between consecutive time points) up to 11 time points, thus the next 10 years from the baseline. For each time point, the prediction was conducted based on all the observed historical values and the predicted or imputed values, if unobserved or missing.

We reported the average test results from 5-fold cross-validation. Specifically, we randomly partitioned the dataset described in Section 2 into three non-duplicated subsets for training, validation, and testing. For rigorous evaluation, we randomly selected 10% of the subjects in each class as the validation set and another 10% as the test set from the baseline time point. At first, we defined the training settings concerning the hyperparameter search space for the learning rate in $\{5 \times 10^{-5}, 5 \times 10^{-4}, 5 \times 10^{-3}, 5 \times 10^{-2}\}$, number of hidden layers in $\{1, 2, 3\}$, size of the hidden units in $\{16, 32, 48, 64, 80, 96\}$, and ℓ_2 -regularization in $\{10^{-6}, 10^{-5}, 10^{-4}, 10^{-3}\}$, respectively. Afterward, the validation set was used to select the hyperparameters. Besides, we utilized an early stopping strategy to find the best hyperparameters by achieving the highest mAUC on the validation set. Subsequently, we used a different strategy for evaluating performance in flawless imputation task and other tasks such as both MRI biomarker and cognitive test scores forecasting, and clinical status prediction. Specifically, as for the imputation task, our experimental setting was inspired by (Cao et al., 2018; Mulyadi et al., 2021). Subsequently, we randomly removed the samples with the rate of $\{5\%, 10\%\}$ observed data from all training, validation, and testing set as the ground truth. Basically, in order to con-

sider the same experimental conditions, when evaluating the competing methods for target tasks, *i.e.*, imputation, regression, and classification, we directly fed the incomplete input features into the network, since their proposed methods have not included the imputation. In other words, for other tasks, we first loaded the optimized model and evaluate task-specific performance, simultaneously. For quantitative evaluation, we used the metrics of MAE and mean relative error (MRE) for the imputation task, MAE for the MRI biomarker prediction task, root mean square error (RMSE) for the cognitive test scores forecasting task, and multi-class area under the receiver operating characteristic curve (mAUC) (Hand and Till, 2001) for the clinical status prediction task. We also conducted statistical significance tests in comparison with the competing methods. Briefly, we used the paired, two-sided Wilcoxon signed-rank test (Wilcoxon, 1992) and Pearson's correlation coefficient for regression tasks, *i.e.*, imputation and MRI biomarkers forecast, on MAE and MRE, while RMSE was used for forecasting cognitive tests. Meanwhile, McNemar's test (McNemar, 1947) on mAUC was applied for the clinical status prediction task.

We compared our proposed method with the following closely-related methods that deal with missing values imputation and prediction tasks:

- Mean imputation with LSTM (LSTM-M) (Wang et al., 2018): Missing values were imputed with the mean values of the respective variables in a training set, and a standard LSTM network was used for MRI biomarker and cognitive test scores forecasting, independently, which were then used for classification with LDA.
- Forward imputation with LSTM (LSTM-F) (Lipton et al., 2016): This is similar to the LSTM-M, except that the missing values were imputed with the most recent observed values.
- Zero imputation with Peephole LSTM (PLSTM-Z) (Ghazi et al., 2019): A peephole LSTM (Gers and Schmidhuber, 2000) was used for MRI biomarker and cognitive test scores forecasting with missing values imputed by zeros as input. The predicted MRI biomarkers and cognitive scores were then used for classification via LDA.
- Multi-directional RNN (MRNN) (Yoon et al., 2018): This operates forward and backward within the intra-stream directions, *i.e.*, for each variable, and in the inter-stream directions, *i.e.*, among variables. Unlike a typical bidirectional-RNN, the timing of inputs into the hidden layers was lagged in the forward direction and advanced in the backward direction. The network outputted the MRI biomarkers and cognitive scores measure for the next time point, which were then fed into LDA for clinical status prediction.
- Model filling with MinimalRNN (MinimalRNN) (Nguyen et al., 2020): By using a MinimalRNN (Chen, 2017), we imputed missing values that could be used to extrapolate features (called a model filling) as input. A MinimalRNN was then used for MRI biomarker and cognitive test scores forecasting, and clinical status prediction, simultaneously. Similar to the forward filling approach, if data was missing at the first time step, the mean value across all time steps of all training subjects was used for the imputation.

For all the competing methods, the optimal hyperparameters were chosen based on the results of the validation set, we set 64 hidden units and trained them using an Adam optimizer (Kingma and Ba, 2014) with a learning rate of 5×10^{-2} (LSTM-M and LSTM-F) and 5×10^{-3} (PLSTM-Z, MRNN, and MinimalRNN), a mini-batch size of 64, a number of hidden layer of 1, and an epoch of 300. To avoid an overfitting problem and make the training curve converge considerably, we applied an ℓ_2 -regularization by setting the corresponding coefficient to 10^{-4} . Regarding the hyperparameters of the composite loss function in Eq. (17), we set them as $\alpha = 0.1$, $\zeta = 0.5$, and $\xi = 0.5$. In Eq. (16), we set $\epsilon = 5$. For the competing methods, for fair comparison, we tried to search for optimal hyperparameters in the composite loss function in Eq. (17) excluding ξ term. Specifically, $(\alpha = 1.0, \zeta = 0.1)$, $(\alpha = 1.0, \zeta = 0.1)$, $(\alpha = 0.25, \zeta = 0.5)$, $(\alpha = 1.0, \zeta = 0.25)$, and $(\alpha = 1.0, \zeta = 1.0)$ were chosen for LSTM-M, LSTM-F, MRNN, PLSTM-Z, and MinimalRNN,

respectively. For evaluation on the test set, we chose the optimal parameters of the comparative networks that achieved the highest mAUC over the validation set. All codes used in our experiments are available at 'https://github.com/ssikjeong1/Deep_Recurrent_AD'.

4.2. Performances

4.2.1. Missing value imputation

We presented the experimental results of the missing values imputation in Table 2. First, in Table 2 (a), it is noteworthy that our proposed method achieved the lowest MAE and MRE scores, outperforming all the competing methods under our consideration with a statistical significance of $p < 0.05$ for all the competing methods. Interestingly, Mean and Forward imputation, which took the simple mean or the last observed values for imputation, achieved relatively better performance than their counterpart method of PLSTM-Z that imputed with zeros and applied a peephole LSTM. Further, as for the MinimalRNN, it could be used to extrapolating the features to fill in missing observations by using a recurrent network. Therefore, the imputation result is similar but better than the Forward imputation. They obtained lower MAE and MRE scores than other competing methods. We believe that imputation of the missing observations during training a recurrent network can result in better classification performance due to considering temporal relations. Besides, as for the MRNN, even though it used the multi-directional information of temporal relations, it reported the highest MAE and MRE scores. Moreover, although both our proposed method and MRNN utilized information sources, *i.e.*, temporal relations, our method further considered missing patterns in M_x and time delay in Δ_t systematically through a series of operations, *i.e.*, multivariate relations, as described in Section 3.2. We believe that this systematic imputation is beneficial and leads to a significantly enhanced performance. We conducted extensive ablation studies on the time delay and missing pattern information and described the results in Section 5.2.

Additionally, we have investigated the imputation results for each of the input features, *i.e.*, both MR volumetric and cognitive test scores features, in Table 2b. When comparing our imputation results with those of the state-of-the-art methods, *i.e.*, MRNN, PLSTM-Z, and MinimalRNN, we observed the following experimental findings of using both MR volumetric and cognitive scores features: Similar to the results of Table 2a, our method also outperformed all competing methods for each feature among MRI and cognitive scores on the MAE metric, showing the least MAE and MRE scores. In the perspective of the feature noise, the experimental results present that our proposed method imputes more accurately and robustly, regardless of which feature is used, compared to other competing methods. Specifically, PLSTM-Z achieved relatively lower performance than their comparative methods since it simply imputed missing values with zeros and applied a peephole LSTM. MRNN reported better performance than PLSTM-Z, which takes advantage of the multi-directional information from temporal relations. Interestingly, MinimalRNN based on a recurrent network for obtaining extrapolate features, achieved the highest MAE and MRE scores among the comparative methods.

4.2.2. MRI biomarker modeling

The forecast errors in MAE over six volumetric MRI biomarkers are presented in Table 3. Unlike the imputation task, LSTM-M and LSTM-F, which used simple imputation, and typical LSTM resulted in relatively higher errors across the MRI biomarkers. However, modeling temporal relations for hidden state representation in MRNN helped to boost performance in Ventricle, Hippocampus, and Whole Brain compared to LSTM-M and LSTM-F. From these findings, it could be hypothesized that the MRI biomarker forecasting was not necessarily helpful for the downstream task. However, our understanding of this phenomenon is that because the amount of longitudinal changes of the MRI biomarker values had been subtle, the simple static values were somehow close to the ground truth on average, but it was not helpful for those simple

Table 2

Performance for an imputation task in terms of MAE and MRE (mean \pm std). The best performance is indicated in boldface. (a) Comparison with all competing methods on MRI features.

Models	MAE	MRE
Mean imputation	$0.235 \pm 0.009^*$	$0.788 \pm 0.062^*$
Forward imputation	$0.062 \pm 0.011^*$	$0.204 \pm 0.043^*$
MRNN (Yoon et al., 2018)	$0.143 \pm 0.014^*$	$0.474 \pm 0.056^*$
PLSTM-Z (Ghazi et al., 2019)	$0.305 \pm 0.015^*$	$1.000 \pm 0.000^*$
MinimalRNN(Nguyen et al., 2020)	$0.119 \pm 0.010^*$	$0.392 \pm 0.041^*$
Ours	0.059 ± 0.005	0.101 ± 0.010

(*: $p < 0.05$)

(b) Comparison with the state-of-the-art methods on both MRI and cognitive scores features.

Models	MAE (top) / MRE (bottom)								
	V	H	WB	EC	FG	MTG	MMSE	ADAS11	ADAS13
MRNN (Yoon et al., 2018)	0.188 0.384	0.137 0.610	0.145 0.812	0.237 0.742	0.154 0.685	0.252 0.913	0.230 0.230	0.847 0.847	0.848 0.848
PLSTM-Z (Ghazi et al., 2019)	0.460 1.000	0.339 1.000	0.179 1.000	0.334 1.000	0.234 1.000	0.188 1.000	1.000 1.000	1.000 1.000	1.000 1.000
MinimalRNN (Nguyen et al., 2020)	0.251 0.518	0.140 0.455	0.146 0.695	0.195 0.617	0.177 0.627	0.149 0.622	0.475 0.475	0.806 0.806	0.790 0.790
Ours	0.075 0.142	0.110 0.381	0.123 0.456	0.143 0.669	0.138 0.679	0.121 0.497	0.116 0.116	0.790 0.790	0.782 0.782

Abbreviation: V, Ventricles; H, Hippocampus; WB, Whole Brain; EC, Entorhinal Cortex; FG, Fusiform Gyrus; MTG, Middle Temporal Gyrus.

Table 3

Performance of forecasting MRI biomarkers one-year later in terms of MAE (mean \pm std). The smallest MAE for each MRI biomarker is highlighted in boldface. (ρ : correlation coefficient)

Models	Ventricles MAE ($\times 10^{-3}$) [ρ]	Hippocampus	Whole Brain	Entorhinal Cortex	Fusiform Gyrus	Middle Temporal Gyrus
LSTM-M (Wang et al., 2018)	$8.20 \pm 1.37^*[0.682]$	$0.51 \pm 0.24^*[0.821]$	$28.98 \pm 16.17^*[0.861]$	$0.26 \pm 0.03^*[0.836]$	$0.87 \pm 0.36^*[0.836]$	$0.81 \pm 0.06^*[0.788]$
LSTM-F (Lipton et al., 2016)	$8.09 \pm 1.15^*[0.698]$	$0.42 \pm 0.08^*[0.859]$	$26.85 \pm 7.22^*[0.813]$	$0.25 \pm 0.07^*[0.784]$	$0.78 \pm 0.13^*[0.786]$	$0.89 \pm 0.09^*[0.834]$
MRNN (Yoon et al., 2018)	$6.25 \pm 1.13^*[0.724]$	$0.41 \pm 0.05^*[0.770]$	$26.58 \pm 2.35^*[0.737]$	$0.31 \pm 0.03^*[0.694]$	$0.90 \pm 0.10^*[0.746]$	$0.96 \pm 0.13^*[0.738]$
PLSTM-Z (Ghazi et al., 2019)	$6.04 \pm 1.19^*[0.795]$	$0.32 \pm 0.05^*[0.873]$	$23.07 \pm 5.96^*[0.842]$	$0.24 \pm 0.01^*[0.834]$	$0.74 \pm 0.12^*[0.860]$	$0.82 \pm 0.11^*[0.834]$
MinimalRNN (Nguyen et al., 2020)	$3.09 \pm 0.61^*[0.874]$	$0.21 \pm 0.03^*[0.902]$	$15.24 \pm 0.66^*[0.936]$	$0.17 \pm 0.03^*[0.801]$	$0.44 \pm 0.08^*[0.869]$	$0.50 \pm 0.12^*[0.856]$
Ours	1.55 ± 0.16 [0.822]	0.14 ± 0.00 [0.905]	11.01 ± 1.22 [0.884]	0.19 ± 0.01 [0.815]	0.41 ± 0.02 [0.880]	0.43 ± 0.05 [0.853]

(*: $p < 0.05$, † : no statistical difference)

static values to capture the temporal and multivariate relations inherent in the data. As for PLSTM-Z, whose major difference from LSTM-M, LSTM-F, and MRNN was the use of a peephole LSTM, it achieved much better MAE scores for all the biomarkers. However, our proposed method⁵ and MinimalRNN were superior to PLSTM-Z. Among them, our proposed method surpassed MinimalRNN in most cases, with margins of 1.54 (ventricles), 0.07 (hippocampus), 4.23 (whole brain), 0.03 (fusiform gyrus), and 0.07 (middle temporal gyrus). From those results, we argue that the piece of masking pattern information played a key role, as discussed in Section 5.2.

4.2.3. Cognitive scores prediction

The forecast errors in RMSE over three cognitive test scores are presented in Table 4. Similar to the MRI biomarker modeling task, LSTM-M and LSTM-F that combined typical LSTM with the simple imputation method resulted in relatively higher errors across cognitive scores. On the other hand, MRNNs that employed temporal relations outperformed the simple imputation methods such as LSTM-M and LSTM-F. From these results, we argue that the cognitive score forecast is associated with

MRI biomarker modeling, and utilizing these features are beneficial for downstream work. It can be inferred that the longitudinal changes of the MRI biomarker values represent morphological changes, and in real clinical practice, the trajectories of the cognitive scores are, reflected in the clinician's opinions for judging the patient's disease progression. As for PLSTM-Z, it achieved much better RMSE scores for all the biomarkers than others (LSTM-M, LSTM-F, and MRNN). However, in contrast to the MRI biomarker modeling task, MinimalRNN outperformed PLSTM-Z in only MMSE scores. In the case of other cognitive scores, i.e., ADAS-cog11 and ADAS-cog13, PLSTM-Z outperformed the MinimalRNN. Similar to the MRI biomarker modeling task, our proposed method⁶ achieved much better RMSE scores than all of the competing methods for all the cognitive test scores, with margins of 0.745 (0.113), MMSE, compared to MinimalRNN, 1.139 (0.976), ADAS-cog11, and 1.679(1.523), ADAS-cog13, compared to PLSTM-Z.

4.2.4. Clinical status prediction

In the clinical status prediction task, due to a high imbalance in sample sizes among the three classes of AD, MCI, and CN, we additionally

⁵ The yearly detailed performance of our method is presented in Table D1.

⁶ The yearly detailed performance of our method is presented in Table D1.

Table 4

Performance of predicting cognitive scores in terms of RMSE. The smallest RMSE value for each cognitive score is highlighted in boldface. (ρ : correlation coefficient)

Models	MMSE (Baseline)		ADAS-cog11 (Baseline)		ADAS-cog13 (Baseline)	
	RMSE	ρ	RMSE	ρ	RMSE	ρ
LSTM-M (Wang et al., 2018)	6.825±1.522* (8.854±3.898)	0.432	8.902±2.603* (8.235±4.080)	0.651	11.544±2.146* (12.542±4.038)	0.675
LSTM-F (Lipton et al., 2016)	6.078±3.018* (8.943±4.079)	0.382	7.510±0.676* (8.154±3.315)	0.645	10.730±1.888* (11.946±5.001)	0.722
MRNN (Yoon et al., 2018)	3.758±0.614* (3.951±0.559)	0.616	7.208±1.191* (8.344±2.191)	0.674	9.514±1.551* (11.529±2.690)	0.685
PLSTM-Z (Ghazi et al., 2019)	3.490±0.621* (2.929±0.505)	0.698	5.449±0.913* (5.269±1.682)	0.833	6.986±0.983* (6.971±1.997)	0.847
MinimalRNN (Nguyen et al., 2020)	3.064±1.389† (2.294±0.082)	0.741	7.406±2.832† (4.652±0.305)	0.672	8.310±2.437* (5.798±0.426)	0.692
Ours	2.319±0.123 (2.181±0.096)	0.863	4.310±0.210 (4.293±0.825)	0.900	5.307±0.202 (5.448±0.706)	0.916

(*: $p < 0.05$, † : no statistical difference)

Table 5

Performance on a multi-class (AD vs. MCI vs. CN) classification task (mean±std). The best performance in each metric is highlighted in boldface.

Models	mAUC	Recall	Precision
LSTM-M (Wang et al., 2018)	0.758±0.034***	0.501±0.201	0.577±0.218
LSTM-F (Lipton et al., 2016)	0.741±0.018***	0.549±0.162	0.521±0.107
MRNN (Yoon et al., 2018)	0.774±0.045***	0.611±0.045	0.580±0.092
PLSTM-Z (Ghazi et al., 2019)	0.842±0.035***	0.706±0.092	0.636±0.093
MinimalRNN (Nguyen et al., 2020)	0.871±0.015**	0.743±0.091	0.644±0.083
Ours	0.878±0.022	0.723±0.071	0.710±0.071

(***: $p < 0.001$, **: $p < 0.01$)

reported precision and recall, along with mAUC, in **Table 5**. Notably, like the MRI biomarker and cognitive test score forecast, LSTM-M and LSTM-F based on the standard LSTM architecture were inferior to the other competing methods. Among the comparative methods, PLSTM-Z (Ghazi et al., 2019) resulted in boosted performance in all metrics of mAUC, recall, and precision. Meanwhile, MinimalRNN outperformed PLSTM-Z by achieving high scores in mAUC, recall, and precision. Similar to the MRI biomarker modeling and cognitive score prediction task, our proposed method⁷ outperformed all the competing methods by achieving the highest scores in mAUC and precision with margins of 0.007 and 0.066, respectively, compared to MinimalRNN. From those results in **Section 4.2.2**, **4.2.3**, and **4.2.4**, we argue that if the predictive model has obtained higher performance in both MRI biomarker modeling and cognitive scores prediction, the predictive model may achieve a more accurate performance in the classification task.

5. Discussion

5.1. Effect of multi-task learning

It is noteworthy that in the clinical status prediction task, one of the major differences of our method from the other comparative methods was to jointly optimize the parameters of the MRI biomarker regressor, cognitive scores regressor, and the clinical status prediction classifier. Thus, we also conducted an experiment by modifying our method such that it was trained with a single task of MRI biomarker forecasting and cognitive test scores forecasting, and then independently trained an LDA-based classifier, under the same condition as the comparative models. That is, we trained our model by setting the hyperparameters of $\xi = 0$ ($\alpha = 1.0$, $\zeta = 0.75$) in the composite loss function. We called this variant of the model as single-task learning.

⁷ The yearly computed performance of our method and the respective confusion matrices are presented in **Table D1** and **Fig. D1**, respectively.

In single-task learning, the results of our method were 0.869 ± 0.019 in mAUC, 0.732 ± 0.060 in recall, and 0.672 ± 0.071 in precision, respectively, which are higher than most comparative methods with a margin of 0.111 (vs. LSTM-M), 0.128 (vs. LSTM-F), 0.095 (vs. MRNN), and 0.027 (vs. PLSTM-Z) in terms of mAUC. On the other hand, as for the MinimalRNN result, it is quite similar to our single-task learning performance. Compared to multi-task learning in our proposed method, the joint learning of MRI biomarker forecast, cognitive test scores forecast, and the clinical status prediction helped enhance the performance by 0.009 in mAUC and 0.038 in precision.

5.2. Ablation studies

We first investigated the effect of varying a pair of hyperparameters $\{\alpha, \zeta, \xi\}$ in **Eq. (17)**. We considered these parameters as a ratio to weigh the missing values and future biomarker regression and clinical status classification to achieve optimal performance. For each parameter, we defined a set of range values for these hyperparameters as $\{0.1, 0.25, 0.5, 0.75, 1.0\}$. Based on the highest average AUC score of 0.878 with $\alpha = 0.1$, $\zeta = 0.5$, and $\xi = 0.5$ are chosen.

Our proposed method used a focal loss that considers the imbalance of samples among classes. We varied the value of the hyperparameter ϵ in **Eq. (16)** from 0 to 10 with an interval of 1. The result is presented in **Fig. 3** with a blue solid line. Note that when $\epsilon = 0$, which corresponds to the conventional cross-entropy loss, the mAUC was 0.861 ± 0.018 still outperforming the competing methods excluding the MinimalRNN. Clearly, due to the high imbalance in the number of samples in our training set, it was useful for performance improvement to apply non-zero ϵ values, achieving the highest performance when $\epsilon = 5$.

To validate the effectiveness of using the missingness information, i.e., mask vectors and the time-delay information, and multivariate relation between observations, we also conducted experiments with and without them. The results are shown in **Fig. 3**. With the information on the missingness, our model performed better than with the delay in-

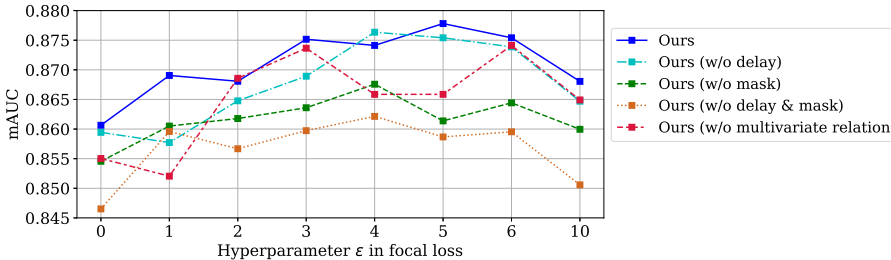


Fig. 3. Result of ablation studies on the effectiveness of the time delay, missingness information, and multivariate relation for the proposed method. In this case, we selected the classification results from the setting of the ϵ value, which is the hyperparameter in the focal loss function.

formation. Moreover, when ignoring both time-delay and missingness information, we achieved the lowest performance over the different experimental settings. We also observed the effect of multivariate relations among observations by showing a volatile performance for the different hyperparameter of ϵ when ignoring multivariate relations. Based on these experimental results, we observed that the effect of multivariate relations was smaller than that of time-delay and missingness information. As a result, we confirmed not only model performance was affected in the order of information on the multivariate relation, time delay, and missingness, but also it showed justification for the proposed method.

5.3. Prediction at multiple time points within a 10-year range

To verify the validity of our proposed method for multiple-time-points prediction, we compared the prognostic performance among MRNN, PLSTM-Z, MinimalRNN, and our method, which ranked in the top four in mAUCs for single next-time-point prediction in [Table 5](#). At each time point, we made clinical status predictions for multiple subsequent time points up to 10 years beyond the baseline with the historical observations and the imputed or predicted values for missing ones. To do this, we divided 10 cases based on the number of historical time points used for clinical status prediction and then measured the mAUC for each case. As an example, for case 5, when having used 5 historical time points, from 0 (baseline) to 4 (4 years), then the clinical statuses over the following 5 time points (5 years) were predicted, along with the MRI biomarker and cognitive test score forecast. The mAUCs of those methods over time are presented with line graphs in [Fig. 4](#). In the figure, we also plotted our proposed method's performance in one-time-point prediction with a dotted blue line for reference. First, from a bias-variance point of view, our proposed method notably showed high (*i.e.*, low-bias) and stable (*i.e.*, low-variance) mAUC scores across the cases. However, MinimalRNN also demonstrated high and stable mAUC scores across the cases. Compared with MinimalRNN, our proposed method was relatively well converged at high scores (mAUC > 0.7) rather than MinimalRNN (mAUC ≈ 0.7) except for the baseline. In addition, there was no tendency for a dramatic decrease in prognosis results over the time steps, which can be regarded as a time-independent property. Meantime, MRNN and PLSTM-Z showed a significant decline over time. Based on these results, our proposed method has learned a robust prognosis result regardless of varying time steps. Second, we found the common characteristics in some prognosis results. That is, the prognostic results for 4 years (short-term) are better for 9 years (long-term) in both our proposed method and MinimalRNN. Furthermore, as used in this experimental setting, when data was accumulated and employed for the disease prognosis task, we observed that the performance was gradually improved. Meanwhile, PLSTM-Z and MRNN showed low mAUC (*i.e.*, high-bias) and unstable mAUC (*i.e.*, high-variance), respectively. Third, the data-driven imputation methods of MRNN, MinimalRNN, and ours were superior to the counterpart method of PLSTM-Z excluding baseline (case 0). As a result, the data-driven imputation methods are relatively robust to predict multiple time points than the method ignoring the missing value, such as PLSTM-Z.

For an early identification of AD progression risk, we also considered the predictive accuracy of our method in terms of conversion-to-AD

within the period of consideration. Based on our 10-year range prognosis, we measured the accuracy and MAE for the conversion-to-AD, and the results are illustrated in

[Fig. 5](#). In the figure, we observed improved accuracies and decreased MAE across cases.

5.4. Irreversible neurodegenerative Alzheimer's disease

The predictive models should also reflect pathological characteristics for the irreversible neurodegeneration of AD. That is, if a subject is under the state of AD at one point, it is not expected for the subject to reverse to MCI or CN in the future. With this consideration, we compared the longitudinal clinical status predictions by MRNN, PLSTM-Z, MinimalRNN, and our proposed method, shown in [Fig. 6](#). In the figure, we presented predictions for six different subjects with different progression types. While MRNN and PLSTM-Z made many state-reversing predictions, our proposed method did not show any such non-acceptable predictions. In the case of MinimalRNN, although MinimalRNN predicted well [Fig. 6 \(c,d,f\)](#) as our proposed method, there are some errors, were misclassified [Fig. 6 \(a,b,e\)](#) and reversed [Fig. 6 \(a,b\)](#). Contrastively, for the subjects with CN ([Fig. 6a](#)) or MCI ([Fig. 6c](#)), our method predicted CN or MCI over the whole period. In [Fig. 6b](#) and [Fig. 6d](#), our method not only predicted earlier disease stage but also not made any state reversing. Moreover, in [Fig. 6d](#), and [Fig. 6e](#), although predictions are misplaced behind by up to three time points, our method did not make any state-reversing predictions.

5.5. Interpreting cell states

While our deep recurrent network achieved relatively superior performance in both MRI biomarker and clinical test scores forecasting, as well as clinical status prediction, it is desirable to understand the dynamics of the internal state representations of our proposed model. In this regard, we devised a novel analysis method of the cell states in our LSTM. To determine which cell states contributed to the identification of the clinical statuses, we estimated the correlation between a patient's disease statuses over time and the corresponding cell state representations. Specifically, we first collected the internal cell representations of ≈ 37 subjects (37.0 ± 8.8 ⁸), who experienced status-conversion during our period of interest, and then measured the correlations between the change of the values in the cell states and a transition of the patient's disease status (0: no conversion and 1: conversion) with point-biserial correlation coefficients. We grouped all subjects depending on the disease transitions as follows: (i) ≈ 7 subjects (7.8 ± 1.7) showed transitions from CN to MCI (CN-MCI), (ii) ≈ 26 subjects (26.8 ± 8.9) showed transitions from MCI to AD (MCI-AD), and (iii) ≈ 2 subjects (2.4 ± 1.4) showed transitions through all the statuses of CN, MCI, and AD (CN-MCI-AD). Then, we analyzed the calculated point-biserial correlations for CN-MCI and MCI-AD.⁹

⁸ This value represented the mean and standard deviation over the number of subjects in 5-fold cross-validation.

⁹ We excluded the CN-MCI-AD group for simplicity in interpretation.

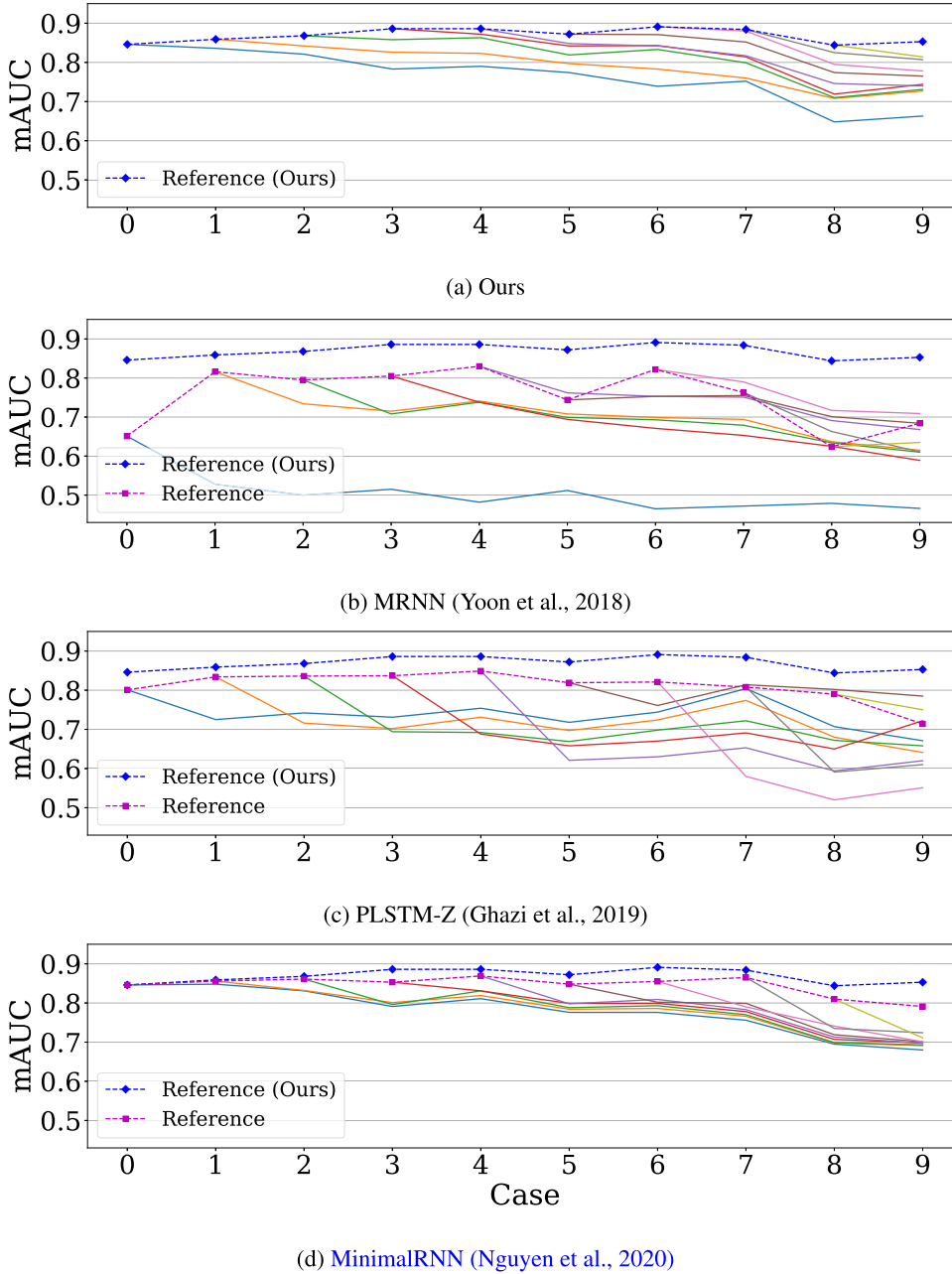


Fig. 4. Disease prognostic results from historical observations between the proposed method, MRNN, PLSTM-Z, and MinimalRNN. From top to bottom, the panels display the disease prognostic performance over time using our method, MRNN, PLSTM-Z, and MinimalRNN. Specifically, the colored solid lines in each panel mean that the patient's disease prognosis results are represented using accumulated data up to that point. In addition, we plotted the comparative method's performance in one-time-point prediction with a dotted magenta line.

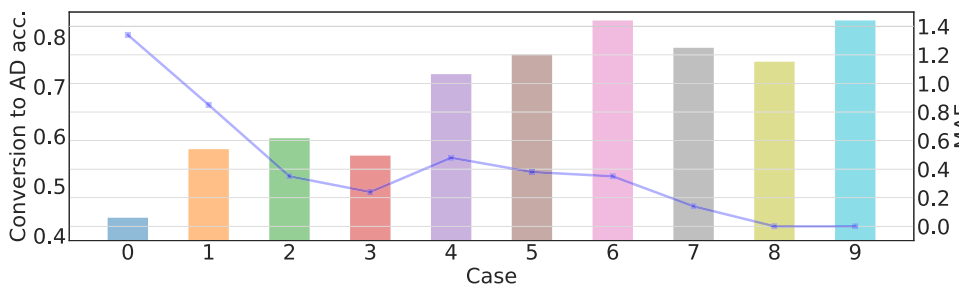


Fig. 5. Conversion-to-AD accuracy for our proposed method. Each box indicates the ability to capture changes in a patient's disease status. Furthermore, the solid line represents the absolute values of the difference between the actual patient label transition time and the model's predictive label conversion time. Note that each case denotes that conversion-to-AD predictions are performed using data accumulated up to that time.

Regarding the variation of conversion time among subjects per group, we normalized the point-biserial correlation coefficients with the standard deviation of the coefficients in each group. Then, we sorted the normalized coefficients to identify the significant cell states related to the transitions, as presented in Fig. E1. From the sorted cells, we focused on cell units with the top 25% most extreme coefficients per group. Of the

selected cell units, the common ≈ 16 cell units (16.6 ± 2.7) in both groups are presented in Fig. 7, where the subfigures correspond to one fold of our five-fold cross-validation experiments. As these cell states showed a high correlations either positively or negatively, we believe that those cell units could be potentially used as '*model biomarkers*' with respect to the clinical status conversion. Interestingly, across the five-fold ex-

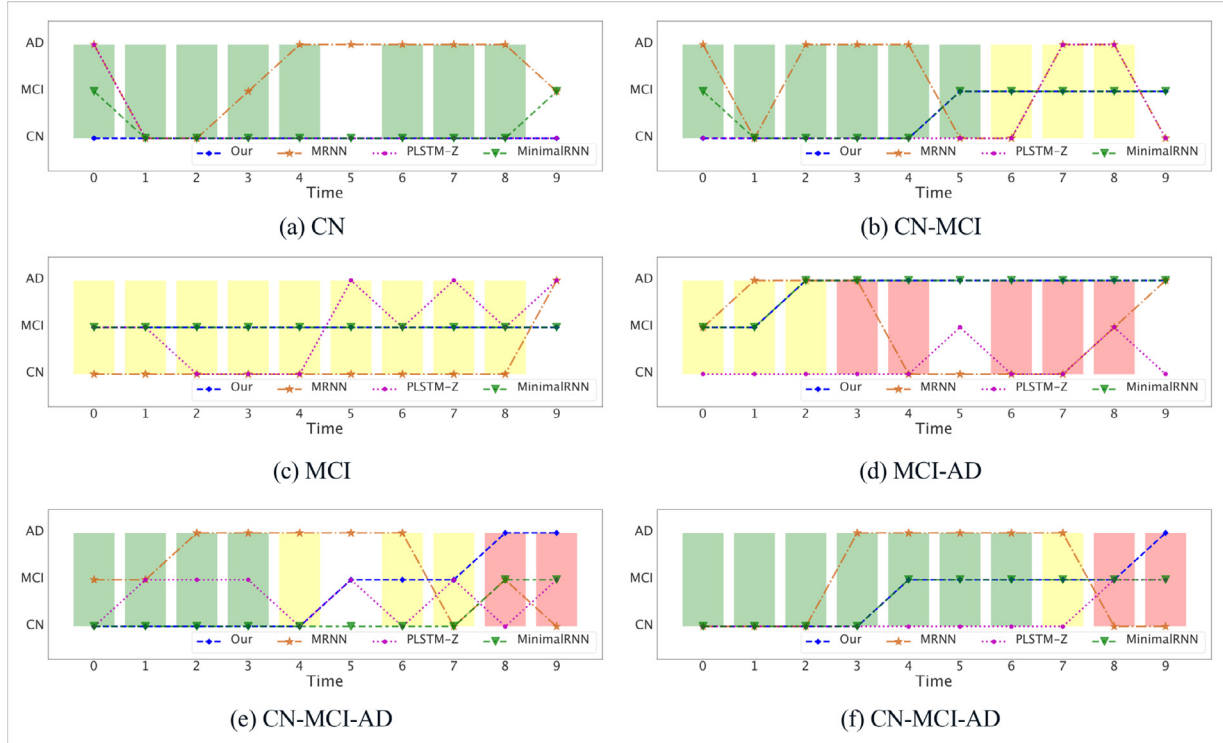


Fig. 6. Results of longitudinal status prediction between the proposed method, MRNN, PLSTM-Z, and MinimalRNN. The plots in each panel represent clinical status conversion from different subjects. Green, yellow, red, and white represent CN, MCI, AD, and missing in the true label, respectively.

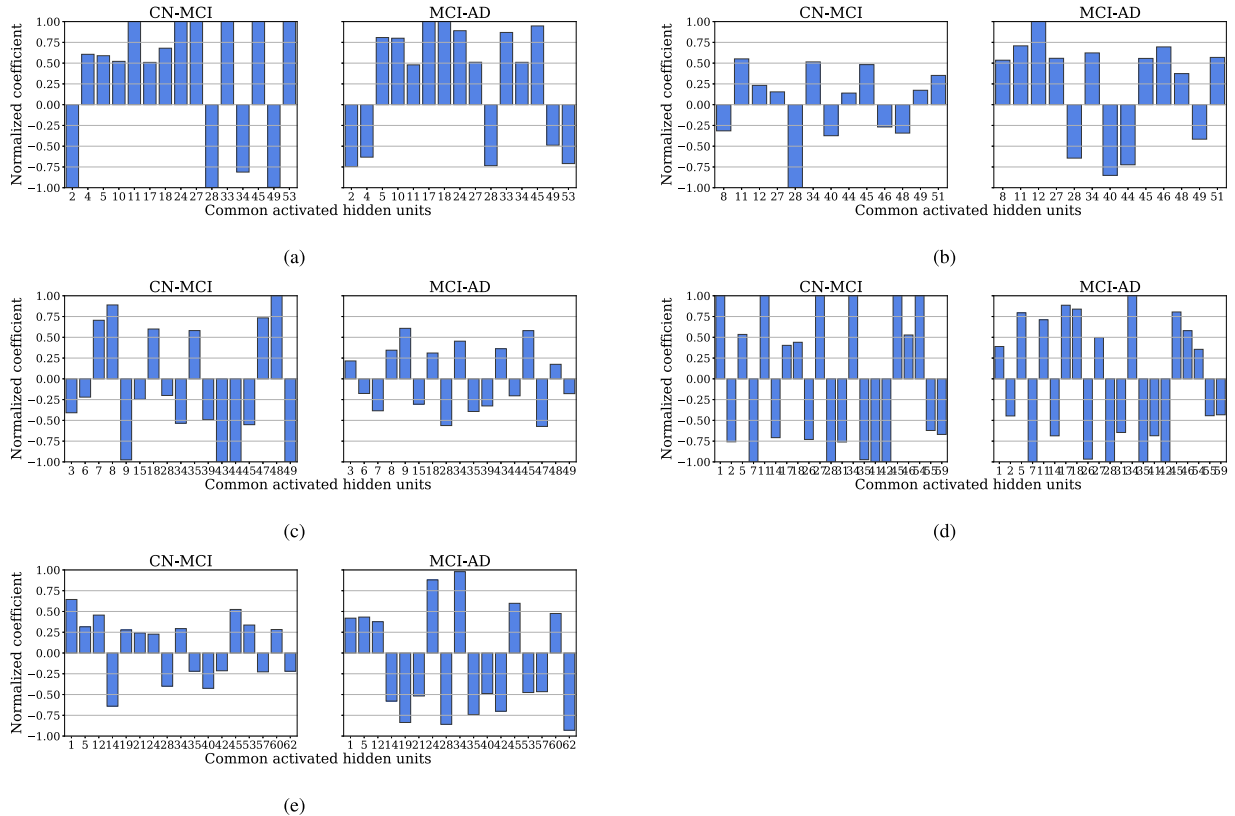


Fig. 7. Normalized point biserial correlation coefficients for subjects with conversions, i.e., CN-MCI and MCI-AD, during a period of 10 years from the baseline. Each panel represents the potential cell units for ‘model biomarkers,’ whose activations were highly correlated with the conversions.

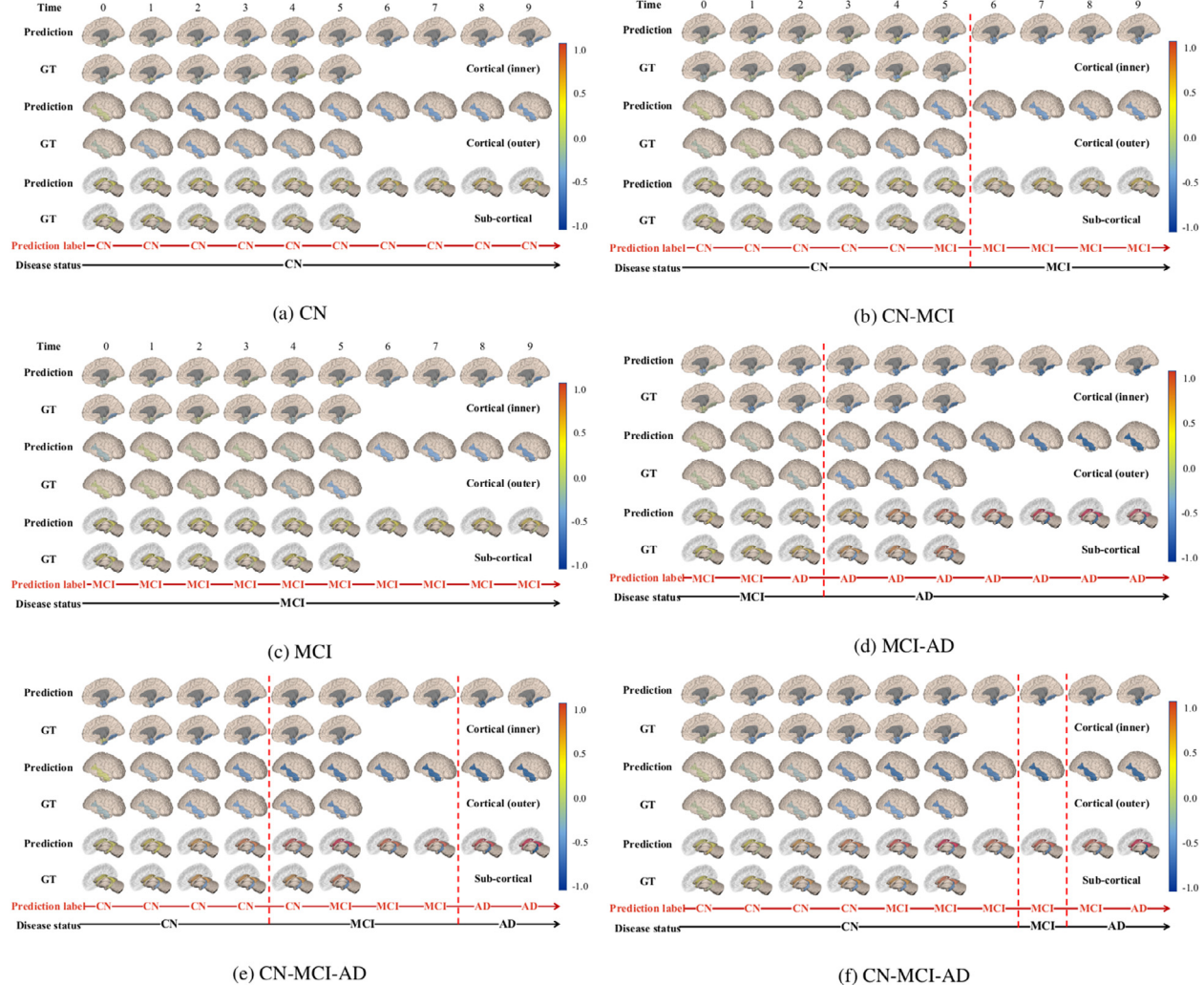


Fig. 8. Examples of individual trajectories of MRI biomarkers are the amount of change over time. The color-coded values indicate the normalized relative changes from the respective regions' values at baseline. (GT: ground truth)

periments, a similar number (13~21) of cell units showed high correlation with the clinical status change. From this observation, we infer the robustness or generalizability of our method over different training sets.

5.6. Individual MRI biomarker value changes over time

In regard to the relationship between the MRI biomarker values and the clinical statuses over time, we visualized the trajectories of MRI biomarker change and the corresponding clinical status in Fig. 8. We computed the relative changes in the prediction (p) and the ground truth (g) from the respective regions' values to the baseline as follows:

$$r_{g,t}^{(i)} = \frac{y_t^{(i)} - y_0^{(i)}}{y_0^{(i)}}, \quad r_{p,t}^{(i)} = \frac{\hat{y}_t^{(i)} - \hat{y}_0^{(i)}}{\hat{y}_0^{(i)}}$$

where i and t denote the indices of MRI biomarkers and time points, respectively. Those relative changes were then normalized with the minimum and maximum values such that the resulting values were in the range of $[-1, 1]$, in which the positive and negative values denote increase and decrease, respectively. As a result, comparing our predictions with the ground truths, they showed very similar values over time and across cases. These experimental results validated our proposed method's ability to forecast the longitudinal MRI biomarkers. Second, unlike the two examples of Fig. 8a and Fig. 8c, which presents stable

or slowly deteriorating status over the period, the regression to other statuses in the AD spectrum (Fig. 8d and Fig. 8e) showed relatively rapid changes in volumetric measurements, i.e., enlarged ventricles and shrunken other (sub)cortical regions.

5.7. Individual cognitive test scores changes over time

Similar to Section 5.6, in regard to the relationship between the cognitive test scores and the clinical statuses over time, in Fig. 9, we visualized the trajectories of the cognitive test scores change and the corresponding clinical status for the same subjects in Fig. 6 and Fig. 8. Note that, in the figure, the cognitive test scores were normalized to [0,1] in the procedure of model training, and we transformed the predicted scores to their original ranges by multiplying max values of the respective cognitive tests, i.e., 30 (MMSE), 70 (ADAS-cog11), and 85 (ADAS-cog13). In comparisons between estimated cognitive scores and the ground truth, the trajectories of the respective cognitive test scores followed the tendency of the ground truth over time and across cases. In addition, we calculated the Pearson correlation between estimated values and ground truth, denoted as ρ in the figure. All cases achieved higher correlation values ($\rho > 0.3$) in Fig. 9. Specifically, we observed high ρ values ($\rho > 0.8$) for disease state changes except for CN-MCI in Fig. 9b showing relatively low MMSE. In addition, in contrast to the four examples of Fig. 9a, Fig. 9b, and Fig. 9c, which showed either rel-

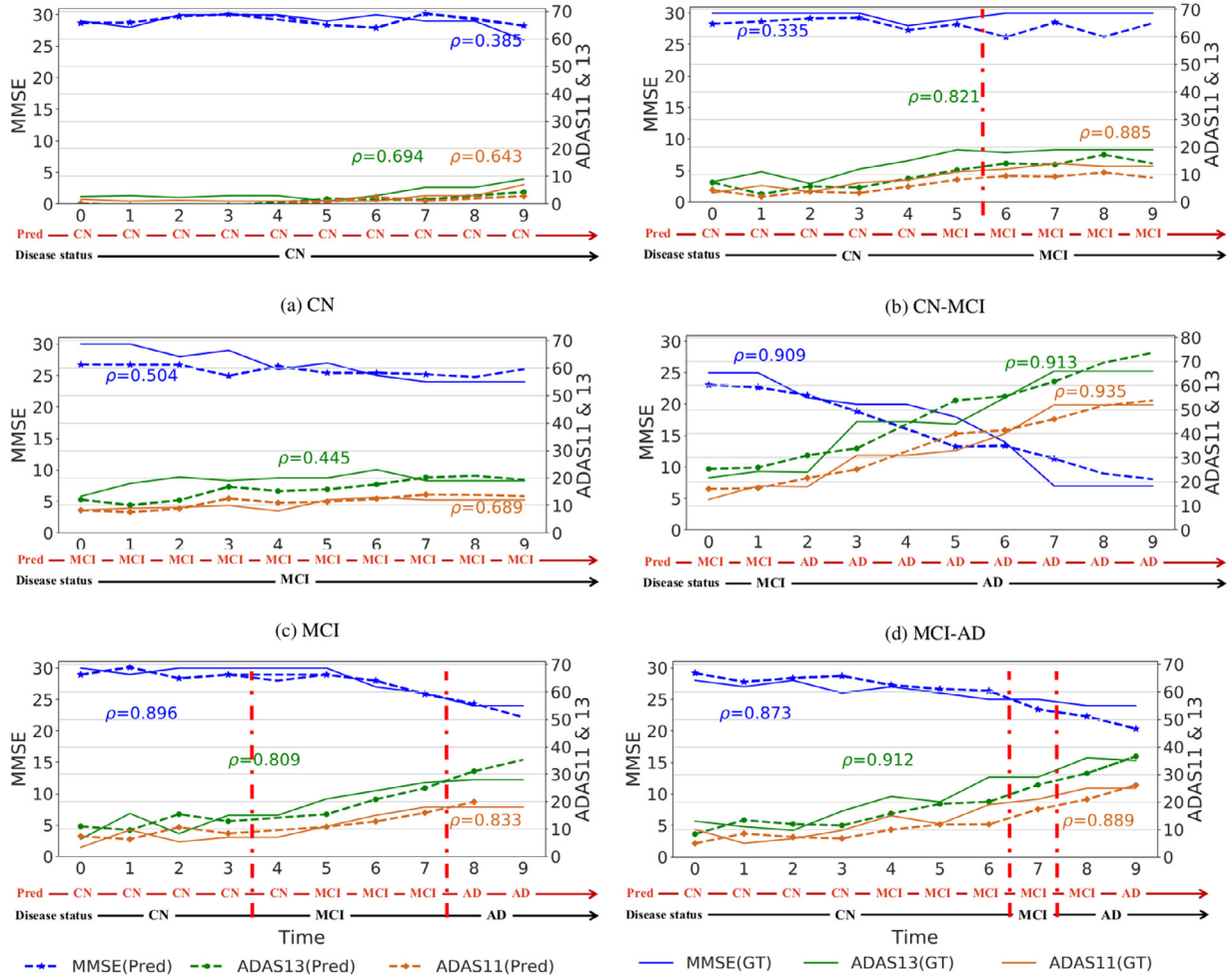


Fig. 9. Examples of individual trajectories of the cognitive tests represents the change of scores over time. Blue, magenta, and chocolate denote MMSE, ADAS-cog11, and ADAS-cog13, respectively. (ρ : correlation coefficient, Pred: prediction, GT: ground truth)

atively stable or slowly decreasing scores over time, the progression to other statuses in the AD spectrum (Fig. 9d, Fig. 9e, and Fig. 9f) represented either dramatically decrease or increase in scores, i.e., decrease in MMSE scores and increase in ADAS-cog11 and ADAS-cog13. As a result, we concluded that our proposed method is capable of capturing the trajectories of the cognitive test scores either stable and slowly degrading the status of the disease or severely deteriorating status.

6. Conclusion

Progressive neurodegenerative AD is of great concern around the world due to its clinical, social, and economic impacts. As there is no treatment or medicine to cure or reverse the progression of AD itself, many researchers in various fields have been devoting their efforts to early diagnosis or prognosis in diverse ways. In particular, the use of neuroimaging data is one of the main areas of study, as it provides quantitative and qualitative measurements on which we can build computational models to predict the risk of AD progression.

Of various strategies for accurate AD diagnosis or prognosis, recent studies on longitudinal datasets validated the significance of using historical observations. In that regard, we formulated the problem of AD progression prognosis, i.e., the tasks of both MRI biomarker and cognitive test score forecasting and clinical status prediction over multi-

ple time points, by means of the disease progression modeling. From a methodological standpoint, we proposed a deep recurrent neural network that is jointly and systematically capable of imputing missing observations, encoding historical inputs into hidden state vector representations, and predicting future MRI biomarker values, cognitive test scores and the respective clinical status. We have performed exhaustive experiments and analyses by comparing with other comparative methods in the literature. First, our proposed method was superior to those competing methods in various quantitative metrics. Second, our method resulted in more stable (low-bias and low-variance) outputs in MRI biomarker forecasting and more reasonable clinical status prediction by reflecting the characteristics of irreversible AD (i.e., no status-reverse prediction was made over time). Third, our method represented the reliable trajectories of the cognitive test scores. Lastly, we observed that some internal state vector representations, i.e., the cell states in our LSTM, showed a high correlation with the clinical state-conversion, implying the potential use of those as ‘model biomarkers’ in predicting clinical status conversion in the near future.

As we considered the six MRI biomarkers and three cognitive test scores in this work, our forthcoming research direction will be to accommodate the MRI biomarkers of the whole brain and to integrate functional and/or genotypic information in multi-modal learning. Further, in order to get new insights about AD progression, it is also important to adopt interpretable and explainable mechanisms in the model.

Code and data availability

All codes used in our experiments are available at 'https://github.com/ssikjeong1/Deep_Recurrent_AD'. We used the TADPOLE longitudinal cohort (<https://tadpole.grand-challenge.org/Data/>) from the publicly available ADNI database, including ADNI-1, ADNI-2 and ADNI-GO.

Declaration of competing interest

The authors declare that they have no conflict of interest.

Credit authorship contribution statement

Wonsik Jung: Conceptualization, Methodology, Software, Validation, Writing - original draft, Visualization, Project administration. **Eunji Jun:** Validation, Writing - review & editing. **Heung-Il Suk:** Conceptualization, Methodology, Supervision, Writing - review & editing, Funding acquisition.

Acknowledgement

This work was supported by Institute for Information communications Technology Planning & Evaluation (IITP) grant funded by the Korea government (MSIT) (No. [2019-0-00079](#), Artificial Intelligence Graduate School Program (Korea University)) and the National Research Foundation of Korea (NRF) grant funded by the Korea government ([MSIT](#)) (No. [2019R1A2C1006543](#)).

Appendix A. Summary of the TADPOLE dataset

Table A1

Demographic information of subjects in the TADPOLE dataset. Values are reported as a mean \pm standard deviation. Note that the number of subjects is measured at the baseline time point and includes missing observation values and clinical statuses during the subject's visits.

Clinical Status	# of subjects		# of visits		Age (mean \pm std.)	
	Male	Female	Male	Female	Male	Female
Cognitively Normal (CN)	253	270	2,126	2,084	75.10 \pm 5.64	74.42 \pm 5.38
Mild Cognitive Impairment (MCI)	515	357	4,207	2,756	73.71 \pm 7.11	71.80 \pm 7.85
Alzheimer's Disease (AD)	189	153	884	684	75.56 \pm 7.11	74.52 \pm 7.81
All	1,737		12,741		73.81 \pm 6.97	

Appendix B. Anatomical regions of the MRI Biomarkers

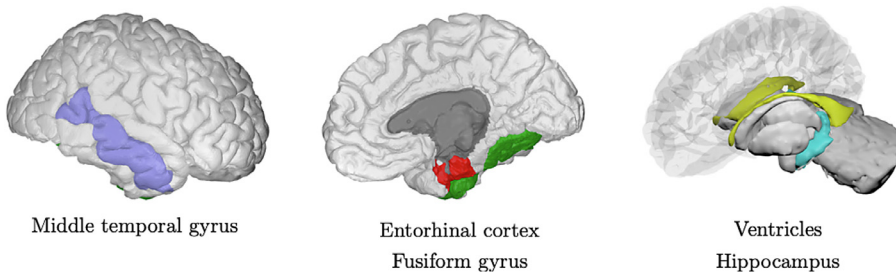


Fig. B1. Visualization of MRI volumetric biomarkers that are used in our experiments. This figure was generated by the BrainPainter ([Marinescu et al., 2019a](#)).

Appendix C. Statistics of the Demographic and Cognitive Scores

Table C1

Statistical information on a demographic and cognitive score for each group every year. Scores on the CDR-SOB, ADAS-cog11, and ADAS-cog13 were higher at severe levels of cognitive dysfunction. Conversely, scores on the MMSE were lower at severe levels of cognitive dysfunction.

Year	Groups	Number (Gender)	Age	MMSE	ADAS-cog11	ADAS-cog13	CDR-SOB
Baseline	CN	226 (M/F: 108/118)	74.0±5.2	29.0±1.1	5.7±2.9	8.8±4.1	0.0±0.1
	MCI	334 (M/F: 289/194)	72.9±7.5	27.4±1.8	10.6±4.7	17.2±6.8	1.5±0.8
	AD	131 (M/F: 63/68)	73.7±7.6	23.2±1.9	18.7±6.8	28.9±8.1	4.2±1.6
1	CN	208 (M/F: 103/105)	73.9±5.3	29.0±1.4	5.2±2.9	8.1±4.3	0.1±0.3
	MCI	275 (M/F: 166/109)	73.5±7.5	27.3±2.3	10.6±5.2	17.0±7.7	1.7±1.1
	AD	177 (M/F: 87/90)	73.0±7.7	21.9±4.0	21.3±8.8	31.9±10.3	5.1±2.4
2	CN	203 (M/F: 105/98)	73.8±5.5	29.2±1.0	5.0±2.7	7.9±4.0	0.1±0.4
	MCI	200 (M/F: 116/84)	73.1±7.3	27.5±2.2	10.1±4.9	16.3±7.4	1.7±1.1
	AD	178 (M/F: 91/87)	73.3±7.7	20.8±5.0	23.4±10.6	34.0±11.5	6.1±3.1
3	CN	126 (M/F: 64/62)	73.7±5.3	29.1±1.3	4.7±2.4	7.7±3.6	0.1±0.3
	MCI	156 (M/F: 95/61)	73.0±7.4	27.5±2.4	9.4±5.0	15.4±7.3	1.6±1.4
	AD	95 (M/F: 48/47)	73.1±6.8	20.9±5.4	22.6±10.1	31.9±9.2	6.2±3.3
4	CN	103 (M/F: 53/50)	73.9±5.8	29.2±1.1	5.7±2.6	8.5±3.7	0.1±0.3
	MCI	99 (M/F: 64/35)	72.6±7.3	27.9±1.9	8.7±3.7	14.1±5.9	1.4±1.2
	AD	70 (M/F: 39/31)	72.3±6.7	20.1±5.2	24.0±11.4	34.8±13.0	6.4±2.9
5	CN	68 (M/F: 33/35)	74.7±5.5	29.0±1.3	5.8±3.0	9.0±4.3	0.1±0.3
	MCI	67 (M/F: 43/24)	72.5±7.0	27.5±2.2	9.2±3.9	15.2±6.5	1.6±1.2
	AD	47 (M/F: 24/23)	71.8±7.0	20.3±5.4	24.8±11.1	35.7±13.2	7.0±3.1
6	CN	64 (M/F: 32/32)	75.0±4.7	28.9±1.5	5.7±2.9	8.9±4.1	0.2±0.3
	MCI	56 (M/F: 40/16)	74.4±6.7	27.5±2.1	9.9±4.9	15.9±7.2	1.7±1.5
	AD	42 (M/F: 22/20)	72.6±6.8	18.2±6.3	26.9±13.9	38.5±15.7	8.1±3.9
7	CN	49 (M/F: 26/23)	74.7±4.2	29.1±1.3	5.1±2.9	8.2±4.2	0.2±0.4
	MCI	52 (M/F: 34/18)	74.5±6.3	27.7±1.8	9.8±4.5	15.8±7.1	1.4±1.1
	AD	30 (M/F: 15/17)	71.4±6.4	18.2±5.7	28.4±12.4	40.4±13.8	8.8±3.8
8	CN	34 (M/F: 16/18)	75.1±4.7	28.9±1.2	5.6±2.7	9.3±3.9	0.2±0.4
	MCI	34 (M/F: 24/10)	74.1±6.5	27.6±2.5	10.3±4.8	16.2±6.9	1.5±1.0
	AD	28 (M/F: 17/11)	73.0±6.9	19.2±6.6	25.5±12.4	37.4±15.0	7.3±3.8
9	CN	22 (M/F: 13/9)	73.5 ±3.6	29.2±1.3	5.1±2.4	7.8±3.5	0.1±0.3
	MCI	25 (M/F: 15/10)	73.4±5.8	28.2±2.1	8.9±3.5	14.1±5.6	1.2±1.2
	AD	23 (M/F: 14/9)	74.1±6.1	19.4±5.0	22.6±8.3	33.8±10.5	6.7±4.1
10	CN	13 (M/F: 4/9)	74.9±4.0	28.8±1.2	5.5±3.0	9.4±4.6	0.1±0.2
	MCI	19 (M/F: 14/5)	75.7±5.8	27.3±2.1	11.1±5.3	17.1±7.8	1.8±1.5
	AD	10 (M/F: 6/4)	72.5±4.6	20.9±7.0	26.0±12.6	36.9±15.5	7.2±2.8

* Age, MMSE, CDR-SB, ADAS-cog11, and ADAS-cog13 are listed as (Mean ± Standard deviation).

* Abbreviation: AD, Alzheimer's disease; ADAS-cog, Alzheimer's Disease Assessment Scale-cognitive subscale; CDR-SOB, Clinical Dementia Rating scale-Sum of the Boxes; CN, Cognitively Normal; F, Female; M, Male; MCI, Mild Cognitive Impairment; MMSE, Mini-Mental State Examination.

Appendix D. Performance across Time

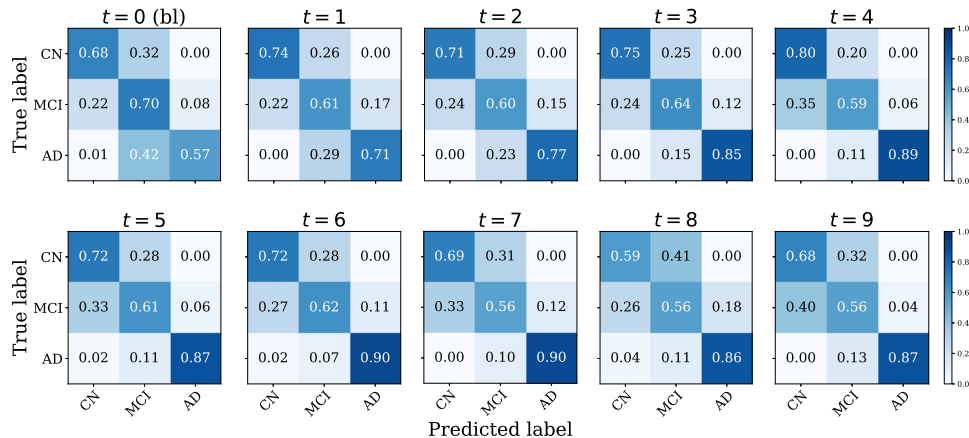


Fig. D1. Yearly computed multi-class classification confusion matrices with normalization using our proposed method. The diagonal elements are the number of points where the predicted labels were the same as the real labels, excluding missing labels, whereas the non-diagonal elements were misclassified by our proposed method. The higher the diagonal value and the darker the shade of blue, the more accurate is the diagnosis of the clinical status.

Table D1

Longitudinal classification and regression results for each year in each of the specific volumes for the brain and the cognitive test scores. We observed that the data imbalance was caused over time but the performance did not change significantly. Additionally, the MAE of cognitive test values decreased and the accuracy of classification increased over time. Lastly, we observed the patterns between cognitive score decline and clinical status prediction accuracy.

Year	0	1	2	3	4	5	6	7	8	9
# of subjects										
CN	226	208	203	126	103	68	64	49	34	22
MCI	334	275	200	156	99	67	56	52	34	25
AD	131	177	178	95	70	47	42	30	28	23
MRI Biomarker Regression (MAE)										
Ventricles	1.972	1.952	2.257	2.427	2.906	2.874	2.282	2.566	3.590	2.961
Hippocampus	0.160	0.170	0.159	0.182	0.178	0.177	0.236	0.259	0.154	0.325
Whole Brain	11.489	12.656	11.437	12.987	17.796	17.238	21.905	21.995	8.815	39.245
Entorhinal Cortex	0.205	0.196	0.208	0.223	0.247	0.224	0.254	0.180	0.081	0.622
Fusiform Gyrus	0.477	0.477	0.495	0.509	0.630	0.560	0.470	0.444	0.559	0.399
Middle Temporal Gyrus	0.452	0.465	0.511	0.519	0.571	0.577	0.569	0.537	0.354	0.649
Cognitive Score Regression (RMSE)										
MMSE	2.421	2.409	2.483	2.411	2.640	2.793	2.344	2.303	2.546	2.044
ADAS-cog11	4.676	4.535	4.306	5.065	4.989	5.415	4.488	4.384	4.007	4.328
ADAS-cog13	6.108	5.700	5.435	6.353	6.532	6.412	5.816	5.269	5.567	5.357
AD vs. MCI vs. CN										
mAUC	0.846	0.859	0.868	0.886	0.886	0.872	0.891	0.884	0.844	0.853
Precision	0.652	0.678	0.706	0.735	0.724	0.722	0.757	0.708	0.694	0.677
Recall	0.689	0.695	0.693	0.750	0.792	0.754	0.736	0.710	0.639	0.739

Appendix E. Interpreting Cell States

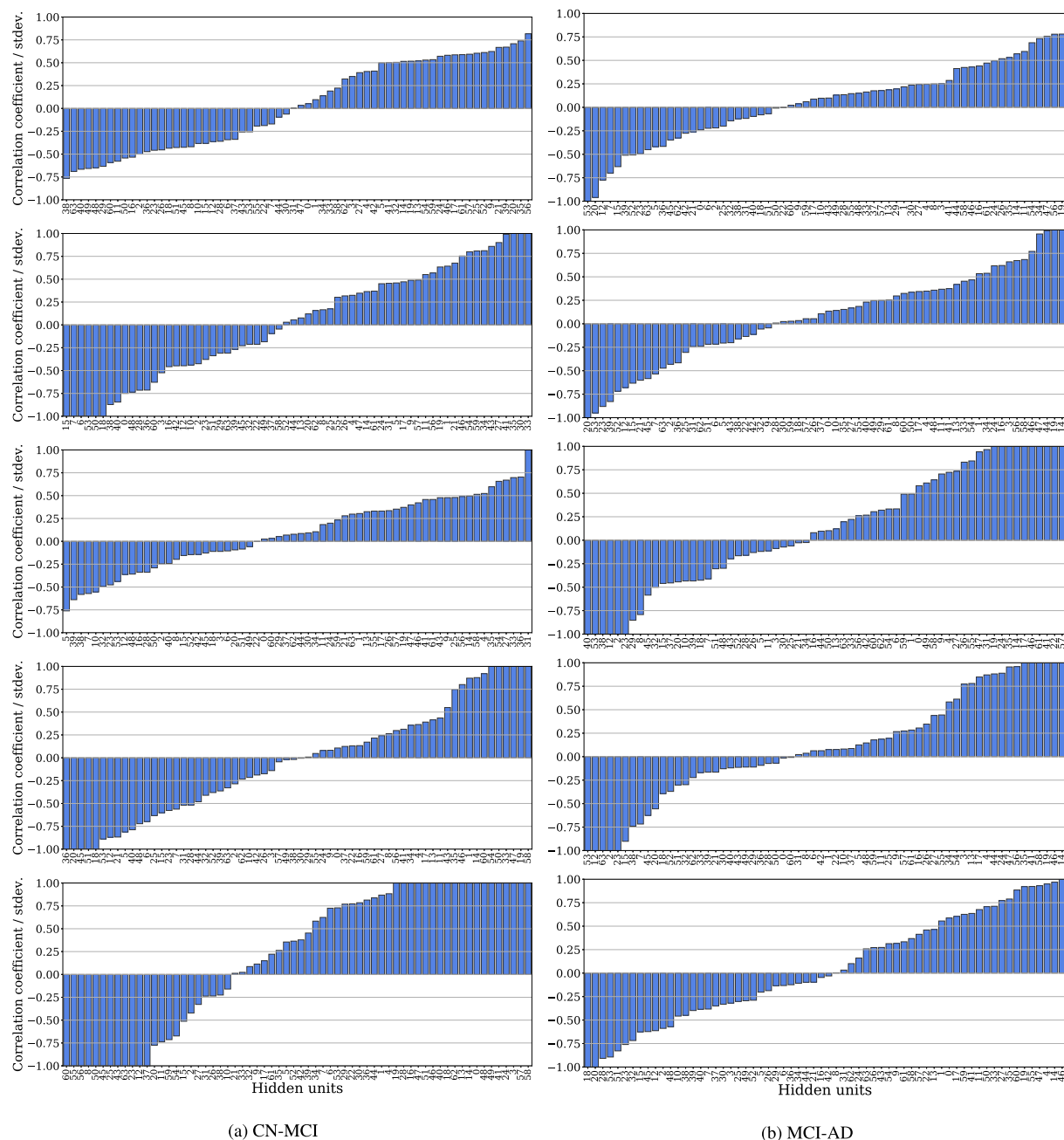


Fig. E1. Normalized point biserial correlation coefficients for subjects with conversion from CN to MCI (left) and from MCI to AD (right) during a period of 10 years from the baseline.

References

- Aghili, M., Tabarestani, S., Adjouadi, M., Adeli, E., 2018. Predictive Modeling of Longitudinal Data for Alzheimers Disease Diagnosis using RNNs. Int. Workshop PRedict. Intell. Med. 112–119.

Albright, J., Alzheimer's Disease Neuroimaging Initiative and others, 2019. Forecasting the progression of Alzheimer's disease using neural networks and a novel preprocessing algorithm. *Alzheimer's Dementia: Transl. Res. Clin. Intervent.* 5, 483–491.

Alzheimer's Association, 2019. 2019 Alzheimer's disease facts and figures. *Alzheimer's Dementia* 15 (3), 321–387.

Ardekani, B.A., Bermudez, E., Mubeen, A.M., Bachman, A.H., 2017. Prediction of incipient alzheimers disease dementia in patients with mild cognitive impairment. *J. Alzheimer's Dis.* 55 (1), 269–281.

Bilgel, M., Jedynak, B., Wong, D.F., Resnick, S.M., Prince, J.L., 2015. Temporal trajectory and progression score estimation from voxelwise longitudinal imaging measures: application to amyloid imaging. *NeuroImage* 134, 658–670.

Braak, H., Braak, E., 1996. Development of Alzheimer-related neurofibrillary changes in the neocortex inversely recapitulates cortical myelogenesis. *Acta Neuropathol.* 92 (2), 197–201.

Brookmeyer, R., Johnson, E., Ziegler-Graham, K., Arrighi, H.M., 2007. Forecasting the global burden of Alzheimers disease. *Alzheimer's Dementia* 3 (3), 186–191.

Cao, W., Wang, D., Li, J., Zhou, H., Li, L., Li, Y., 2018. BRITS: bidirectional recurrent imputation for time series. In: *Advances in Neural Information Processing Systems*, pp. 6775–6785.

Che, Z., Purushotham, S., Cho, K., Sontag, D., Liu, Y., 2018. Recurrent neural networks for multivariate time series with missing values. *Sci. Rep.* 8, 6085.

- Chen, M., 2017. MinimalRNN: toward more interpretable and trainable recurrent neural networks. arXiv preprint arXiv:1711.06788.
- Cheng, D., Liu, M., Fu, J., Wang, Y., 2017. Classification of MR brain images by combination of multi-CNNs for AD diagnosis 10420, 1042042.
- Davis, Wright, 1977. A new method for measuring cranial cavity volume and its application to the assessment of cerebral atrophy at autopsy. *Neuropathol. Appl. Neurobiol.* 3 (5), 341–358.
- Fiot, J.-B., Raguet, H., Risser, L., Cohen, L.D., Fripp, J., Vialard, F.-X., Alzheimer's Disease Neuroimaging Initiative and others, 2014. Longitudinal deformation models, spatial regularizations and learning strategies to quantify Alzheimer's disease progression. *NeuroImage: Clinical* 4, 718–729.
- Gaugler, J., James, B., Johnson, T., Marin, A., Weuve, J., 2019. 2019 Alzheimer's disease facts and figures. *Alzheimers Dementia* 15 (3), 321–387.
- Gers, F.A., Schmidhuber, E., 2001. LSTM recurrent networks learn simple context-free and context-sensitive languages. *IEEE Trans. Neur. Netw.* 12 (6), 1333–1340.
- Gers, F.A., Schmidhuber, J., 2000. Recurrent nets that time and count. In: Proceedings of the IEEE-INNS-ENNS International Joint Conference on Neural Networks, Vol. 3, pp. 189–194vol.3.
- Gers, F.A., Schmidhuber, J., Cummins, F., 1999. Learning to forget: continual prediction with LSTM.
- Ghazi, M.M., Nielsen, M., Pai, A., Cardoso, M.J., Modat, M., Ourselin, S., Sørensen, L., Alzheimers Disease Neuroimaging Initiative and others, 2019. Training recurrent neural networks robust to incomplete data: application to alzheimer's disease progression modeling. *Med. Image Anal.* 53, 39–46.
- Goodfellow, I., Bengio, Y., Courville, A., 2016. Deep learning. MIT Press. <http://www.deeplearningbook.org>
- Gray, K.R., Wolz, R., Heckemann, R.A., Aljabar, P., Hammers, A., Rueckert, D., Alzheimer's Disease Neuroimaging Initiative and others, 2012. Multi-region analysis of longitudinal FDG-PET for the classification of Alzheimer's disease. *NeuroImage* 60 (1), 221–229.
- Guerrero, R., Schmidt-Richberg, A., Ledig, C., Tong, T., Wolz, R., Rueckert, D., Alzheimer's Disease Neuroimaging Initiative and others, 2016. Instantiated mixed effects modeling of Alzheimer's disease markers. *NeuroImage* 142, 113–125.
- Hand, D.J., Till, R.J., 2001. A simple generalisation of the area under the ROC curve for multiple class classification problems. *Mach. Learn.* 45 (2), 171–186.
- Hochreiter, S., Schmidhuber, J., 1997. Long short-term memory. *Neural Comput.* 9 (8), 1735–1780.
- Ibrahim, J.G., Molenberghs, G., 2009. Missing data methods in longitudinal studies: a review. *Test* 18 (1), 1–43.
- Iddi, S., Li, D., Aisen, P.S., Rafii, M.S., Thompson, W.K., Donohue, M.C., Alzheimers Disease Neuroimaging Initiative and others, 2019. Predicting The course of alzheimers progression. *Brain Inf.* 6 (1), 6.
- Jung, W., Mulyadi, A.W., Suk, H.-I., 2019. Unified modeling of imputation, forecasting, and prediction for AD progression. In: International Conference on Medical Image Computing and Computer-Assisted Intervention. Springer, pp. 168–176.
- Kingma, D.P., Ba, J., 2014. Adam: a method for stochastic optimization. arXiv preprint arXiv:1412.6980.
- Lee, G., Nho, K., Kang, B., Sohn, K.-A., Kim, D., 2019. Predicting Alzheimers disease progression using multi-modal deep learning approach. *Sci. Rep.* 9 (1), 1–12.
- Lin, T.-Y., Goyal, P., Girshick, R., He, K., Dollár, P., 2017. Focal loss for dense object Detection 2980–2988.
- Lipton, Z.C., Kale, D.C., Wetzel, R., 2016. Modeling missing data in clinical time series with RNNs. *Mach. Learn. Healthcare* 56.
- Liu, M., Cheng, D., Yan, W., Alzheimers Disease Neuroimaging Initiative and others, 2018. Classification of Alzheimers disease by combination of convolutional and recurrent neural networks using FDG-PET images. *Front. Neuroinformatic*. 12, 35.
- Liu, M., Zhang, J., Adeli, E., Shen, D., 2018. Joint classification and regression via deep multi-task multi-channel learning for Alzheimer's disease diagnosis. *IEEE Trans. Biomed. Eng.* 66 (5), 1195–1206.
- Lorenzi, M., Filippone, M., Frisoni, G.B., Alexander, D.C., Ourselin, S., Alzheimer's Disease Neuroimaging Initiative and others, 2019. Probabilistic disease progression modeling to characterize diagnostic uncertainty: application to staging and prediction in Alzheimer's disease. *NeuroImage* 190, 56–68.
- Lu, P., 2019. Statistical learning from multimodal genetic and neuroimaging data for prediction of Alzheimer's disease. Sorbonne Université.
- Marinescu, R.V., Eshaghi, A., Alexander, D.C., Golland, P., 2019. BrainPainter: a software for the visualisation of brain structures, biomarkers and associated pathological processes. In: Multimodal Brain Image Analysis and Mathematical Foundations of Computational Anatomy. Springer, pp. 112–120.
- Marinescu, R.V., Eshaghi, A., Lorenzi, M., Young, A.L., Oxtoby, N.P., Garbarino, S., Crutch, S.J., Alexander, D.C., Alzheimer's Disease Neuroimaging Initiative and others, 2019. DIVE: a spatiotemporal progression model of brain pathology in neurodegenerative disorders. *NeuroImage* 192, 166–177.
- Marinescu, R.V., Oxtoby, N.P., Young, A.L., Bron, E.E., Toga, A.W., Weiner, M.W., Barkhof, F., Fox, N.C., Klein, S., Alexander, D.C., et al., 2018. TADPOLE challenge: prediction of longitudinal evolution in alzheimer's disease. arXiv preprint arXiv:1805.03909.
- McNemar, Q., 1947. Note on the sampling error of the difference between correlated proportions or percentages. *Psychometrika* 12 (2), 153–157.
- Miller Jr, R.G., 2011. Survival analysis, Vol. 66. John Wiley & Sons.
- Mills, K.L., Tamnes, C.K., 2014. Methods and considerations for longitudinal structural brain imaging analysis across development. *Dev. Cognit. Neurosci.* 9, 172–190.
- Misra, C., Fan, Y., Davatzikos, C., 2009. Baseline and longitudinal patterns of brain atrophy in MCI patients, and their use in prediction of short-term conversion to AD: results from ADNI. *NeuroImage* 44 (4), 1415–1422.
- Morris, J., Storandt, M., McKeel, D., Rubin, E., Price, J., Grant, E., Berg, L., 1996. Cerebral amyloid deposition and diffuse plaques in "Normal" aging: evidence for presymptomatic and very mild Alzheimer's disease. *Neurology* 46 (3), 707–719.
- Mulyadi, A.W., Jun, E., Suk, H.-I., 2021. Uncertainty-aware variational-recurrent imputation network for clinical time series. *IEEE Trans. Cybernet.*
- Nestor, S.M., Rupsingh, R., Borrie, M., Accomazzi, V., Wells, J.L., Fogarty, J., Bartha, R., Alzheimer's Disease Neuroimaging Initiative, 2008. Ventricular enlargement as a possible measure of Alzheimer's disease progression validated using the Alzheimer's disease neuroimaging initiative database. *Brain* 131 (9), 2443–2454.
- Nguyen, M., He, T., An, L., Alexander, D.C., Feng, J., Yeo, B.T., Alzheimer's Disease Neuroimaging Initiative and others, 2020. Predicting Alzheimer's disease progression using deep recurrent neural networks. *NeuroImage* 222, 117203.
- Oulhaj, A., Wilcock, G.K., Smith, A.D., de Jager, C.A., 2009. Predicting the time of conversion to MCI in the elderly: role of verbal expression and learning. *Neurology* 73 (18), 1436–1442.
- Oxtoby, N.P., Alexander, D.C., 2017. Imaging plus X: multimodal models of neurodegenerative disease. *Curr. Opin. Neurol.* 30 (4), 371.
- Oxtoby, N.P., Young, A.L., Cash, D.M., Benzinger, T.L., Fagan, A.M., Morris, J.C., Bateman, R.J., Fox, N.C., Schott, J.M., Alexander, D.C., 2018. Data-driven models of dominantly-inherited Alzheimer's disease progression. *Brain* 141 (5), 1529–1544.
- Patterson, C., 2018. World Alzheimer report 2018: the state of the art of dementia research: new frontiers. *Alzheimer. Dis. Int. (ADI)*: London, UK.
- Petersen, R.C., Aisen, P., Beckett, L.A., Donohue, M., Gamst, A., Harvey, D.J., Jack, C., Jagust, W., Shaw, L., Toga, A., et al., 2010. Alzheimer's disease neuroimaging initiative (ADNI): clinical characterization. *Neurology* 74 (3), 201–209.
- Peterson, K., Rudovic, O., Guerrero, R., Picard, R.W., 2017. Personalized gaussian processes for future prediction of Alzheimer's disease progression. arXiv preprint arXiv:1712.00181.
- Shi, B., Chen, Y., Zhang, P., Smith, C.D., Liu, J., Alzheimer's Disease Neuroimaging Initiative and others, 2017. Nonlinear feature transformation and deep fusion for Alzheimer's disease staging analysis. *Pattern Recognit.* 63, 487–498.
- Suk, H.-I., 2017. An introduction to neural networks and deep learning. In: Deep Learning for Medical Image Analysis. Elsevier, pp. 3–24.
- Suk, H.-I., Lee, S.-W., Shen, D., Alzheimer's Disease Neuroimaging Initiative and others, 2014. Hierarchical feature representation and multimodal fusion with deep learning for AD/MCI diagnosis. *NeuroImage* 101, 569–582.
- Suk, H.-I., Lee, S.-W., Shen, D., Alzheimer's Disease Neuroimaging Initiative and others, 2016. Deep sparse multi-task learning for feature selection in Alzheimers disease diagnosis. *Brain Struct. Func.* 221 (5), 2569–2587.
- Suk, H.-I., Shen, D., 2013. Deep learning-based feature representation for AD/MCI classification. In: International Conference on Medical Image Computing and Computer-Assisted Intervention. Springer, pp. 583–590.
- Suk, H.-I., Shen, D., Alzheimers Disease Neuroimaging Initiative and others, 2015. Deep learning in diagnosis of brain disorders. In: Recent Progress in Brain and Cognitive Engineering. Springer, pp. 203–213.
- Sukkar, R., Katz, E., Zhang, Y., Raunig, D., Wyman, B.T., 2012. Disease progression modeling using hidden markov models. In: 2012 Annual International Conference of the IEEE Engineering in Medicine and Biology Society. IEEE, pp. 2845–2848.
- Thung, K.-H., Yap, P.-T., Adeli, E., Lee, S.-W., Shen, D., Alzheimer's Disease Neuroimaging Initiative and others, 2018. Conversion and time-to-conversion predictions of mild cognitive impairment using low-rank affinity pursuit denoising and matrix completion. *Med. Image Anal.* 45, 68–82.
- Venkatraghavan, V., Bron, E.E., Niessen, W.J., Klein, S., Alzheimer's Disease Neuroimaging Initiative and others, 2019. Disease progression timeline estimation for Alzheimer's disease using discriminative event based modeling. *NeuroImage* 186, 518–532.
- Wang, T., Qiu, R.G., Yu, M., 2018. Predictive modeling of the progression of Alzheimers disease with recurrent neural networks. *Sci. Rep.* 8 (1), 9161.
- Wei, R., Li, C., Fogelson, N., Li, L., 2016. Prediction of conversion from mild cognitive impairment to Alzheimer's disease using mri and structural network features. *Front. Aging Neurosci.* 8, 76.
- Wilcoxon, F., 1992. Individual comparisons by ranking methods. *Breakthrough. Stat.* 196–202.
- Yoon, J., Zame, W.R., Van der Schaar, M., 2018. Estimating missing data in temporal data streams using multi-directional recurrent neural networks. *IEEE Trans. Biomed. Eng.* 66 (5), 1477–1490.
- Zhang, D., Shen, D., Alzheimer's Disease Neuroimaging Initiative and others, 2012. Predicting future clinical changes of mci patients using longitudinal and multimodal biomarkers. *PLoS One* 7 (3).
- Zhang, D., Wang, Y., Zhou, L., Yuan, H., Shen, D., Alzheimer's Disease Neuroimaging Initiative and others, 2011. Multimodal classification of Alzheimer's disease and mild cognitive impairment. *NeuroImage* 55 (3), 856–867.